Applications in Energy and Combustion Science 24 (2025) 100403

Contents lists available at ScienceDirect

Applications in Energy and Combustion Science

journal homepage: www.sciencedirect.com/journal/applications-in-energy-and-combustion-science

Fuel reid vapor pressure level and ethanol content on stochastic preignition, effects at steady and unsteady engine operation

Derek A. Splitter [a,*], Gurneesh Jatana [a], Dan DelVescovo [b], Gina Fioroni [c], Elana Chapman [d], John Salyers [d], Johnathan Pung [d], Scott Parrish [d]

[a] Oak Ridge National Laboratory, 2360 Cherahala Blvd., Knoxville, TN 37932, USA
[b] Oakland University, 115 Library Dr., Rochester, MI 48309, USA
[c] National Renewable Energy Laboratory, 15013 Denver W. Pkwy., Golden, CO 80401, USA
[d] General Motors, 850N. Glenwood Ave., Pontiac, MI 48340, USA

ARTICLE INFO

Keywords:
Low-speed preignition
LSPI
Stochastic preignition
SPI
Fuel RVP
Ethanol
Ignition

ABSTRACT

The present work investigates relations between fuel Reid vapor pressure (RVP) and biofuel (ethanol) content on stochastic preignition (SPI) at both sustained steady-state engine operation and following load transients. This work stems from in-field observations that automotive original equipment manufacturers have observed consistent seasonal increases in United States customer drivability complaints and warranty claims during September and October where SPI is suspected to be responsible. The seasonal timing of these events coincides with the United States seasonal fuel property changeover initiating on September 15 each year, where fuel RVP increases. To explore potential linkage between fuel RVP and SPI the present study employs engine SPI experiments coupled with laboratory spray measurements of fuels with RVPs of 8, 12, and 16 psi in both E10 (10% ethanol) and E25 (25% ethanol) fuels.

Engine results are partitioned into fuel RVP and ethanol content effects on SPI in steady-state, sustained high-load engine operation and unsteady-state low- to high-load transitions, where off-engine spray vessel patternation and tip penetration results help to elucidate the observed fuel effects on SPI. A boosted direct-injected, spark-ignition engine was fueled with three market relevant E10 and E25 fuels with RVPs of 8, 12, and 16 to characterize the interplay between winter fuels and abnormal combustion behavior. The steady-state work shows that for high-load, steady-state engine operation, SPI is directly linked to fuel retention, which was found to be dependent on fuel distillation. The unsteady-state engine operation work shows that following low-to high-load transitions, SPI can occur from a memory of fuel property effects at low-load operation. Specifically, the fuel RVP effect on fuel spray collapse at low loads was found to correlate with SPI with a more than 95% confidence interval following low- to high-engine-load transitions. Results suggest that fuel-wall impingement at low-load operation could carry over into high-load transitions and generate SPI events following low- to high-load transitions.

1. Introduction

Stochastic preignition (SPI) is an undesirable abnormal combustion process where combustion initiates from an uncontrolled source before the commanded spark discharge. SPI can result in severe knocking—including super and mega knock events—and thus limits the

Abbreviations: λ_{mass}, intake air and fuel flow-based lambda; λ_{exh}, exhaust oxygen sensor-based lambda; ΔP, constant pressure differential; AFR, Air-to-fuel ratio; AFR_{CBE}, Air-to-fuel ratio carbon balance error; ASTM, ASTM International (formerly American Society for Testing and Materials); CA, crank angle; CA05, crank angle at 5% mass fraction burned; CA50, crank angle at 50% mass fraction burned; CARB, California Air Research Board; COD, coefficient of determination; E10, 10% by volume ethanol; E25, 25% by volume ethanol; EIA, Energy Information Agency; FiL, fuel in lube; FiO, fuel in oil; FME, fuel mass error; FMR, fuel mass retained; FWI, fuel-wall impingement; GDI, gasoline direct injection; HoV, heat of vaporization; IMEPg, gross indicated mean effective pressure; NREL, National Renewable Energy Laboratory; PCP, peak cylinder pressure; PMI, particulate matter index; RVP, Reid vapor pressure; SCE, single-cylinder engine; SI, spark ignition; SOI, start of injection; SMD, Sauter mean diameter; SPI, stochastic preignition; TDC, top dead center; TRZ, top ring zone.

* Corresponding author.
E-mail address: splitterda@ornl.gov (D.A. Splitter).

https://doi.org/10.1016/j.jaecs.2025.100403
Received 23 May 2025; Received in revised form 5 September 2025; Accepted 30 September 2025
Available online 1 October 2025

potential for engine downsizing [1]. Such events can lead to catastrophic engine failure, making SPI a significant contributor to manufacturer warranty claims [2].

Due to its serious consequences, SPI has been studied extensively for over a decade to understand the factors influencing its occurrence. Despite many investigations revealing mechanistic insights, the fundamental chemistry and physics linking fuel, lubricant, and engine operating conditions remain unclear [2–9]. Chapman et al. [10]. reviewed decades of abnormal ignition in gasoline engines, focusing on preignition, and highlighted that SPI is not limited to boosted engines. Instead, SPI depends strongly on fuel properties, engine design, and operation. A critical finding and current knowledge gap identified in that work is the governing factors surrounding the SPI initiation source. Specifically, why and what fuel and lubricant properties are important from a detailed fundamental chemical–physical nature in relation to SPI promotion or inhibition is an outstanding knowledge gap. In efforts to help bridge known gaps recent research has focused on the effects of in-cylinder mixing process and lubricant properties that have been linked to increased SPI [11,12]. To that extent, SPI has been closely linked between engine operating conditions and the composition of both fuel and lubricants [11,13–20].

Studying SPI is challenging because it is a stochastic process that requires diligence in conditions and experimental approach. Correspondingly, research targeting different approaches to assess SPI have occured [21], where variations in approach have shed light on the fundamentals of SPI.

One leading theory for SPI initiation is liquid ejection from the top ring zone (TRZ) due to fuel-wall interaction. Gasoline direct injection (GDI) engines can exhibit fuel-wall wetting/interaction which can be affected by injection timing and fuel properties [5]. Recently, Splitter et al. (2021a, 2021b) [22,23] utilized a laser-induced fluorescence diagnostic to measure engine lubricant fuel dilution from fuel-wall impingement in GDI engines. Further details on the diagnostic approach and design are described in detail in Neupane et al. [24]. where prior work by Parks et al. established the foundational proof-of-concept [25]. The combined works on the diagnostic showed that fuel-wall impingement was a function of both engine load (i.e., fuel mass) and start-of-injection (SOI) timing. More recently Splitter et al. (2021a, 2021b) [22,23] demonstrated via direct measurements that fuel-wall impingement can increase at high engine loads and/or at retarded SOI timings. Splitter et al. (2021a) [22] specifically suggested through simulation work coupled to experimental measurements, that the preferential vaporization of fuel species may play a role in the speciation of retained top ring zone liquids.

Building on these findings, the present study investigates fuel-wall interaction on SPI during steady-state operation and following low-to-high load transients. It specifically examines how fuel Reid vapor pressure (RVP) and biofuel content (ethanol) could affect fuel-wall interaction and thus SPI rates. While fuel RVP has not traditionally been linked to SPI, observed seasonal spikes in drivability complaints and warranty claims in the U.S. during September and October suggest a possible connection to seasonal RVP changes.

In the United States, gasoline RVP is regulated by the EPA [26]. The Clean Air Act Section 211(h) and recent 2020 revisions define the federal RVP regulations in Title 40 CFR §1090.215, which nationally limits summer gasoline RVP to 9.0 psi, as calculated by the ASTM D323 method. However, some localities in the country are subject to a more stringent summer gasoline RVP standard of 7.8 psi, depending on local air quality zonal classifications and standards. Both national and locally mandated RVP limits typically apply at retailers from June 1 to mid-September, with refiners and distributors following slightly different dates (May 1 to September 15 for refiners and distribution terminals). Furthermore, local state specific effects can exist. State-level regulations vary, such as California Air Resources Board (CARB) rules that extend the summer fuel season [27]. Data from CARB has shown that regionally specific fuel property changeover could have an effect on vapor recovery system overpressurization, which in turn can increase fuel vapor fugitive emissions from vehicles and affect air quality [28]. That same study included data that highlighted the steady increase in fuel RVP between 2009 and 2015 in northern and southern California. Fuel RVP of randomly sampled winter blends at retailers increased annually over that 6-year period, with a total increase of more than 1.0 psi at its peak, from approximately 13.42 to 14.58 psi and 11.29 to 12.46 psi in northern and southern California, respectively. CARB also recently moved the fuel transition date earlier (from October 31 to September 28) to allow use of cheaper winter-blend components like butane, as supported by Energy Information Agency data [27,29–31]. While economically motivated, such early transitions may impact abnormal combustion processes like SPI by altering fuel volatility during warmer periods.

Alcohols, which are blended in gasoline to increase fuel octane number and displace petroleum, also affect fuel RVP [32]. With literature demonstrating some alcohols increasing fuel RVP (e.g., ethanol and, even more significantly, methanol) [33]; while slightly longer C3 alcohols like 1-proponal did not affect RVP, and C4 and above alcohols such as 1-butanol decreased fuel RVP [34]. In fact, because of the nonlinear relationship between ethanol and fuel RVP, the EPA historically has allowed a 1.0 psi waiver to E10 blends, and more recently, E15 blends [35], to account for such effects. However, this waiver was recently modified by the EPA in 40 CFR §1090 as a result of specific state requests, eliminating the waiver in Illinois, Iowa, Minnesota, Missouri, Nebraska, Ohio, South Dakota, and Wisconsin, effective in 2025 [36].

Ethanol's effects on SPI are complex and have been studied extensively as highlighted in a review work by Rönn et al. [37]., which documented that some studies showed increasing SPI with ethanol content [38,39], and others showed a decreasing or complex relationship with ethanol content, especially at midlevel blends [40–42]. The conflicting findings of ethanol's effects on SPI is believed to be coupled with its increased enthalpy of vaporization as compared to gasoline [43], which is suspected to increase fuel films from reduced vaporization rates [41]. When fuel impinges on lubricant-wetted surfaces at engine relevant temperatures, the evaporation process can be slowed compared with the same process on dry surfaces [44], supporting the idea of retained fuel films contributing to SPI. This impingement and evaporation process is less understood ethanol containing fuels as the increased enthalpy of vaporization and relatively low boiling point of ethanol are conflicting effects. Ethanol also exhibits thin reaction zones in the gas phase, which can increase abnormal ignition propensity, promoting SPI [8]. Additionally, the base fuel composition affects SPI with ethanol blends: higher distillation components in the base fuel increase fuel retention and SPI, although these blends may still have lower SPI than ethanol-free fuels [42]. It should be noted that in that work (and the current work), fuel retention refers to the difference between the measured carbon balance from the engine exhaust and the direct air-fuel measurements supplied to the engine, and is not directly a measurement of oil-fuel dilution (which can be a result of over fueling). Thus, in Splitter et al. [42], the fuel retention findings highlight that base-fuel composition (i.e., if an increase in high-distillation components occurs) and the ethanol content of the fuel seem to be critical factors in ethanol SPI propensity.

Besides ethanol's effects, SPI testing procedures themselves exhibit complexities. A well-accepted theory is that foreign ignition sources arise from the TRZ, either from fuel-wall interaction or other mechanisms [21]. Much of the prior research on SPI has been conducted under steady-state engine operating conditions, but recent work by Moriyoshi et al. [45], found that transient load changes and reduced ring pack tension can eject TRZ liquids and trigger SPI with more pronounced transient effects than steady operation. Field tests by Michlberger et al. [46]. confirmed the increase in SPI during rapid load transitions, especially when the engine reaches its maximum boost. Conversely, laboratory testing by Haenel et al. [47]. showed that a slow controlled load increase did not inherently trigger SPI, highlighting the possible need for

a rapid transition to trigger SPI. Relf et al. [48]. saw similar results when employing the test developed by Haenel et al. [47].. Hanel et al. also noted ethanol blends influence SPI but found no bias during slow transitions. These findings indicate that fuel retention at low loads affects SPI during low-to-high load transitions.

A suspected SPI source during rapid load changes is fuel-wall adhesion at low load, which carries over during transients. Fuels with higher volatility (high ethanol or RVP) exhibit spray collapse under sub-atmospheric conditions at elevated fuel temperatures, [49–51] which is linked to vapor pressure relative to ambient pressure [49,52,53]. Splitter et al. (2021b)[22]demonstrated that isooctane causes more fuel spray impingement than E10 gasoline at low-to-intermediate loads and delayed injection timings, linking spray dynamics to fuel-wall interaction [22]. Combining observations of increased SPI with rapid load changes, fuel spray collapse with volatile fuels, and higher fuel-wall impingement with volatile fuels, we hypothesize that ethanol content and fuel volatility (i.e. RVP) influence SPI during load transients. This effect may be worsened by premature seasonal RVP transitions when ambient temperatures remain high. To test this hypothesis, we experimentally explore if increasing ethanol from E10 to E25 and or raising fuel RVP from 8 to 12 and 16 psi influence SPI.

The results from this approach are complex, so steady-state and transient operations are analyzed separately. Using laser-induced fluorescence diagnostics developed in prior studies [22–25,42], fuel-wall impingement is measured to investigate fuel retention effects on SPI. Results in the present work show that at steady-state operation, fuel distillation and associated fuel retention were found to have the most significant influence on SPI at sustained high-load operation. Interestingly, however, increased fuel-wall retention did not inherently correlate with increased fuel-wall impingement. That is fuels with increased fuel-wall impingement did not necessary exhibit increased fuel wall retention. Specifically, fuels with an increased distillation (i.e., energy fraction) above the liner wall temperature increased fuel retention and thus SPI propensity. Moreover, the E25 fuels increased fuel-wall impingement, but the increased RVP fuels seemed to decrease fuel-wall retention. Thus, at sustained high-load engine operation, the distillation effects and associated fuel retention ultimately dominated SPI propensity more than merely fuel-wall impingement.

In contrast, following low-to-high load transitions, fuel RVP was found to be a more significant factor on SPI. Our analysis suggests that spray collapse of volatile fuels at low load creates a “memory” effect that promotes SPI during load transitions. Thus, in the field, seasonal premature RVP changes and elevated temperatures may intensify this effect.

In summary, this study found that different fuel properties impact SPI depending on the specific operating conditions. While fuel retention underpins SPI sources in both steady and transient operation, fuel spray collapse and increased fuel penetration with high RVP fuels at low load were found to be linked to SPI following low-to-high load transitions, implying distinct time scales and potential “memory” mechanisms for SPI source generation.

2. Methodology

2.1. Fuel-in-lube diagnostic

A laser-induced fluorescence optical diagnostic tool developed by Neupane et al. [24]. – termed a fuel-in-lube (FiL) diagnostic –was used in this study. The FiL instrument relies on the intra-spray transport of a dye (Model TP-3400, Tracerline) to the cylinder liner where it is retained and drops out into the engine lubricant circuit. Prior work [42,54] highlighted that at 75 ppm dye doping, no measurable effects of the dye on fuel properties within the ASTM International testing uncertainties were present. Neupane et al. shows detailed specifics of the instrument and approach [24]. Despite prior evidence that 75 ppm dye did not affect the fuel properties within ASTM standard uncertainties, the present work dyed fuel in only some of the tests to ensure that neither the dye itself nor the process of dying the very high RVP fuels affected this study. For each fuel, at least one test—the middle in a triplicate series of tests—was dyed.

Table 1
Specifications for the engine used in this study.

Bore (mm)	86
Stroke (mm)	86
Connecting rod (mm)	145
Compression ratio	9.2:1
Number of valves	4
Displaced volume (L)	0.495
Exhaust valve lift (mm)	10.2
Exhaust valve duration (°CA)	188
Inlet valve lift (mm)	10.2
Intake valve duration (°CA)	200
Direct injector	Side-mounted
Rail pressure (bar)	100

2.2. Engine

A single-cylinder engine (SCE) was used in the present work. Starting with a production GM 2.0 L Ecotec LNF engine, three of the cylinders were deactivated (cylinders 1–3) and the camshafts on those cylinders were ground to the base circle and the intake and exhaust ports were blocked. In the fired cylinder (cylinder 4), the geometry of the combustion chamber and camshaft profile were unaltered. For all engine tests, the production side–mounted direct injector with six holes of 232-micron diameter each arranged in an asymmetric pattern was used with 100 bar of fuel rail pressure. The engine specifications are presented in Table 1.

A layout of the experiential setup is depicted in Fig. 1, where a dry-sump oiling system is also seen. The dry-sump enabled the FiL measurements to be made prior to the scrape down of the lubricant diluting with the sump oil. A 351 hp alternating-current dynamometer (DyneSystems) was used to control the load and speed of the engine. All tests were performed at 2000 rev/min engine speed. An oversized steel flywheel was used to mitigate torque pulsations (12 in. diameter, 3 in. thick).

Air to the SCE engine was supplied by a mass flow controller (Alicat 2000 SLPM). This approach delivers a known mass of air and allows the intake pressure to float as a function of engine speed and volumetric efficiency. An air dryer was used to condition the supplied intake air to a relative humidity of below 10 % at 35 °C. The air was controlled to 35 °C at the intake using a heater. A back-pressure valve (Flowserve Series 75) was used downstream of the exhaust surge tank to maintain a constant ΔP of 15 kPa between the intake and exhaust plenums (intake higher than exhaust). This approach enabled replication of real turbocharging conditions with a combined turbocharger efficiency of approximately 35 % [55].

The exhaust air-to-fuel ratio (AFR) was monitored and maintained using closed loop control via a pressure-compensated lambda sensor (ECM EGR 5220) installed in the laboratory-specific exhaust manifold. The supplied AFR to the engine were also calculated simultaneously using the commanded air mass flow, and a Coriolis-based fuel flow meter (Micro Motion ELITE CMF010P). Lastly, the exhaust emissions based AFR on an oxygen and carbon basis were also calculated and cross verified with the lambda-based measurement using the emissions bench measurements.

For fuels with RVP of 8 or less, fuel supply was provided using a low-pressure lift pump system to supply the production high-pressure, direct-injection fuel pump. A 15 gal (56.8 L) fuel tank with an integral fuel pump (Aeromotive 18,664) coupled with a fuel pressure regulator (Aeromotive 13,128) rated at 4 bar was utilized. Any excess fuel supplied to the regulator was recirculated to the fuel tank through a heat

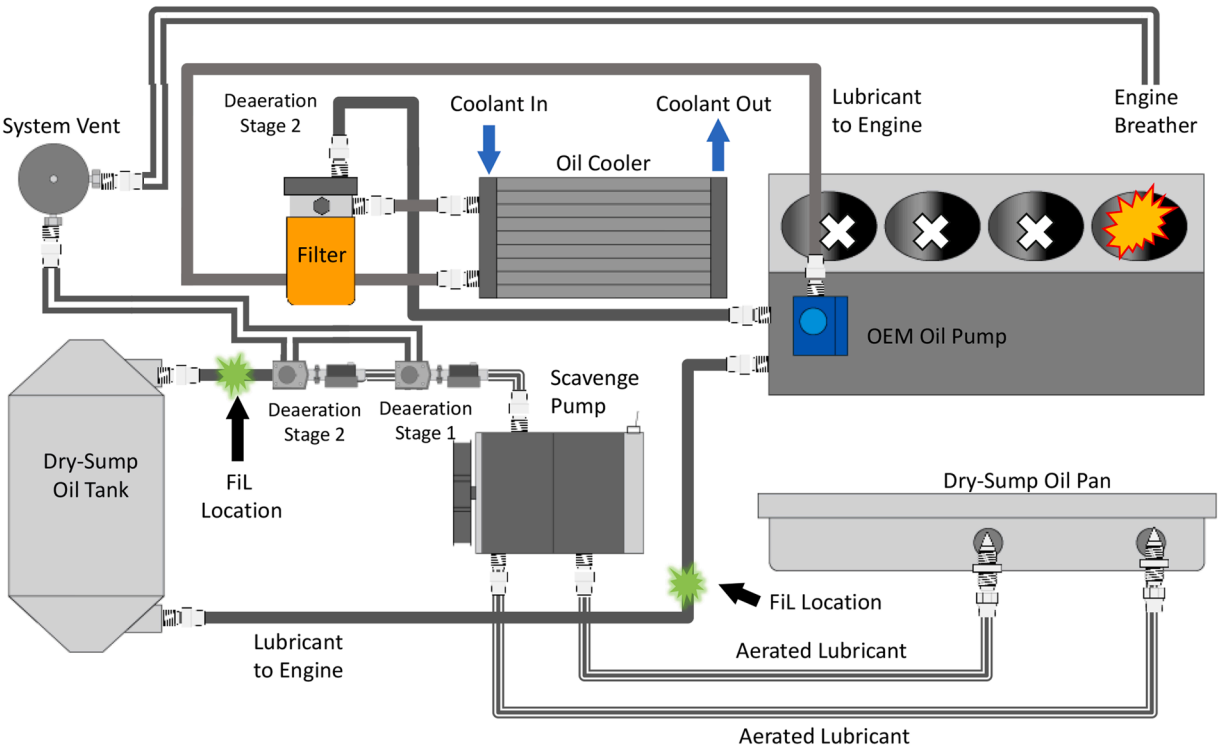

Fig. 1. The diagram illustrates an engine dry-sump oil system with FiL measurement points highlighted in green.

exchanger (Derale 65,860). The fuel stored in the fuel tank was exposed to ambient pressure and temperature conditions.

For fuel with an RVP of 12 psi or greater, a piston accumulator–style fuel system was used, in which pressurized nitrogen at 5 bar supplied fuel to the production high-pressure, direct-injection fuel pump. This system prevented fuel evaporation of the high volatility fuels during testing. Specifics of the accumulator fuel system are provided in greater detail by Szybist et al. [57].

As noted in Fig. 1, extensive modification to the engine lubrication circuit was performed. The production engine oil pump was maintained, but a 2-stage dry-sump scavenge pump and external 3-gallon oil reservoir system were added in place of the production oil sump. Additionally, a high-capacity external oil cooler replaced the production cooler, which was used to maintain a constant temperature. Between the scavenge pump and 3 gal bulk-oil reservoir, the oil passed through two centrifuge style oil-air separators (Spintric III) in series. All tests used both engine coolant and oil temperatures of 75 °C.

A National Instruments–based controller with the Oak Ridge Combustion Analysis System (ORCAS) tool, developed at Oak Ridge National Laboratory was used for engine control and data acquisition. A Kistler pressure transducer (6054BRU59) coupled with an AVL 365C01 encoder with a crank resolution of 0.2 °CA were used for indicating combustion analysis in ORCAS.

2.3. Lubricant

The experimental campaign used an SAE 5W-30 synthetic GF-5 lubricant with a calcium level between 2000 and 2500 ppm. To prevent cross-contamination the oil was triple-flushed, and the filters were changed after every SPI test. Lubricant mass filled and drained from the engine was measured at every oil change using a scale (Sartorius CP34001S). Oil draining was performed immediately after SPI testing while the lubricant was still hot.

2.4. SPI characterization

In this work, SPI cycles were identified using a dedicated combustion analysis subroutine written in MATLAB using otherwise unprocessed heat-release data calculated during engine operation using ORCAS. Unprocessed data were used to maintain a consistent data analysis routine between steady-state and unsteady engine operation.

SPI events were determined using the approach described by Mansfield et al. [58]. However, in the present work only statistically early combustion events—using a 5 % mass fraction burned crank angle

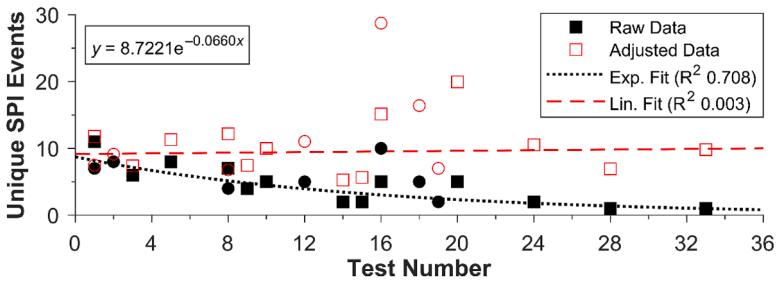

Fig. 2. Raw and age-adjusted PACE 20 SPI event totals as a function of test number for the two engines used in this work are shown, engine 1 are square markers, engine 2 are circle markers, along with exponential decay fit of the raw data and linear fit of the adjusted data.

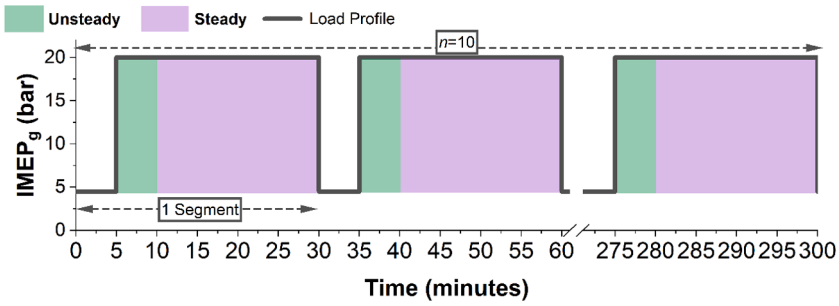

Fig. 3. The SPI test operating schedule used in this study shows unsteady (green) and steady (purple) portions of the test cycles.

(CA05) metric— were used to flag cycles that indicated SPI. SPI identification based on statistically high peak pressure, early combustion, and the conflation of high peak pressure and early CA05 yielded practically identical findings in this study.

A four standard deviations from the mean of CA05 criteria was used to flag SPI cycles, which was determined to be statically robust. Only unique SPI are presented in this study, where events separated by less than or equal to 10 consecutive cycles were classified as only a single event, a method consistent with that in Splitter, Colomer et al. (2023) [42].

Lastly, SPI events were corrected for engine age, a well-established approach outlined by others in prior work in order to provide a consistent baseline for SPI response tendencies across fuels tested at different times [56]. In the present work, all SPI counts were adjusted for engine age using the SPI response of a given fuel relative to PACE 20 (the baseline fuel) at a given engine age. Fig. 2 shows the exponentially decaying tendency (R^2 of 0.657) of SPI event frequency as a function of test number (analogous to engine age) for the PACE 20 control fuel for the two different engines used in the present work. For all fuels, raw SPI counts were adjusted to account for engine age using the relationship shown in Eq. (1), where $SPI_{test_i,fuel_j}$ is the raw event total for a given fuel j corresponding to test i, and $AC_{test_i,fuel_j}$ is the adjusted SPI count for the given fuel and test. Fig. 2 shows the raw and age-adjusted SPI event counts for PACE 20, highlighting the degradation of SPI counts with engine age in the raw data and the relatively consistent counts after the age adjustment was applied.

$$AC_{test_i,fuel_j} = \frac{SPI_{test_i,fuel_j}}{\exp(-0.0660 \times test_i)} \quad (1)$$

2.5. Operating conditions

All tests were conducted at 2000 rev/min following the automated test cycle shown in Fig. 3, which consisted of ten square-waved load profile segments. Each segment is characterized by 5 min of low-load operation (5 bar IMEP$_g$), followed by 25 min of high-load operation (approximately 20 bar IMEP$_g$). During the high-load operation portion, the first 5000 cycles were analyzed separately from the last 20,000 cycles because of the duration required for thermal transients, as discussed in Splitter et al. (2017) [7]. Thus, the analysis generates two parallel data sets for each 10-segment test. One data set in the present analysis is the steady-state results from the last 20,000 cycles for each segment, while the second data set is from the first 5000 cycles of each segment in the 10-segment test, representing the unsteady portion of the test. Both data sets will be explored in the present work.

An absolute intake airflow of 1250 g/min (which corresponded to an absolute intake pressure of approximately 205 kPa$_a$) was held constant. The corresponding engine load achieved was approximately 20 bar gross indicated mean effective pressure (IMEP$_g$). One SOI timing and one coolant temperature were used in this study: 220 °CA bTDC$_f$ and 75 °C, respectively. The engine coolant temperature was intentionally operated colder than that of fully warm conditions, and the SOI timing was intentionally retarded to 220 °CA bTDC$_f$; as these were operating

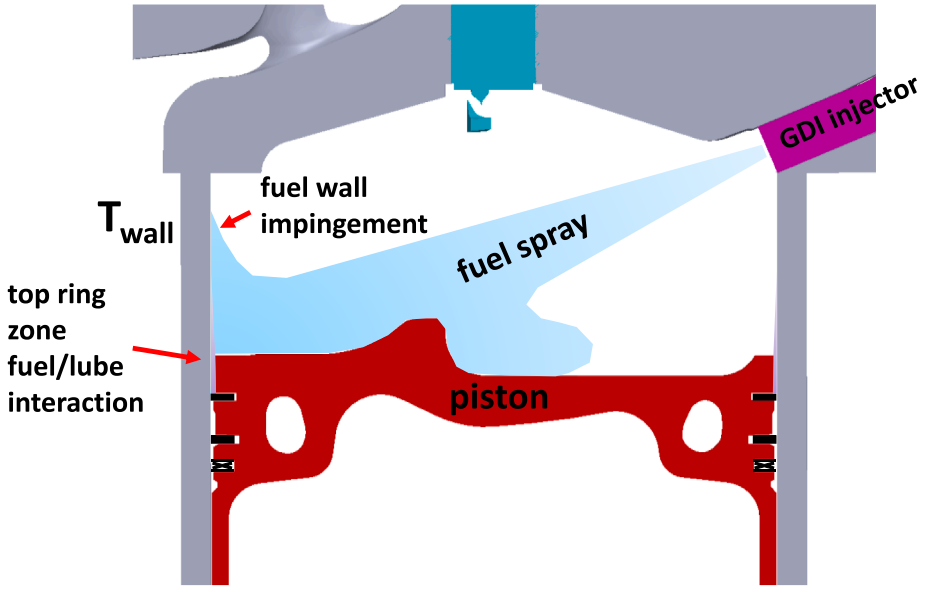

Fig. 4. This schematic illustrates the fuel-wall impingement concept at high fueling rates required for high load where SPI is observed. (GDI: gasoline direct injection.).

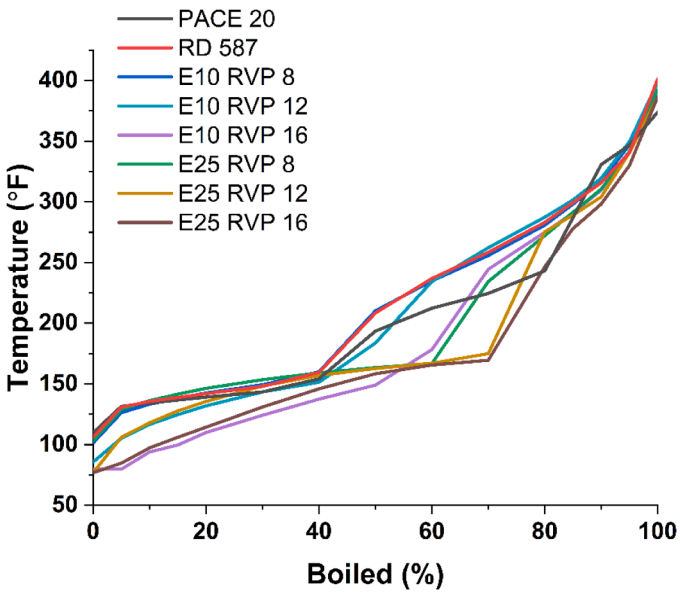

Fig. 5. ASTM D86 data are shown for the fuels used in this study.

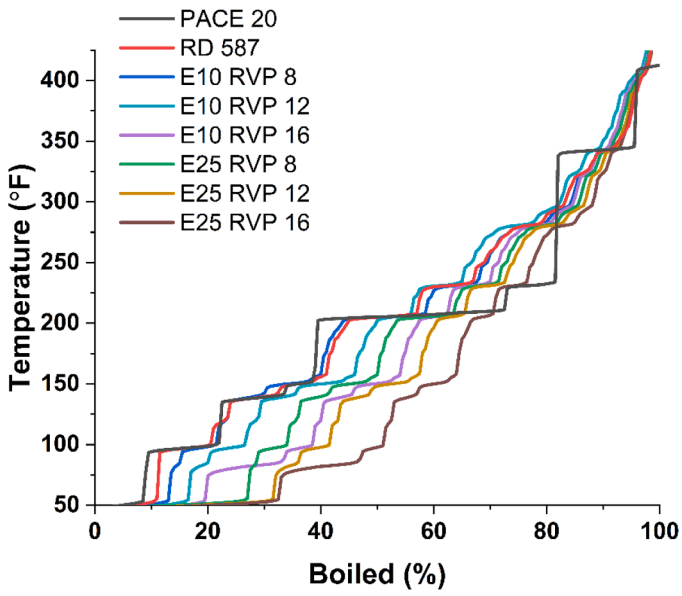

Fig. 6. The simulated distillation of the fuels used in this study is categorized by ethanol content and RVP.

conditions previously established for this laboratory setup to promote SPI [42]. For all fuels, the CA50 timing was held constant at 33 °CA aTDC$_f$ via spark advance adjustments. The generality of the associated fuel wall spray targeting—and the associated impingement generated by these conditions and load—is shown in Fig. 4, which highlights the fuel-wall impingement possible at the 220 °CA bTDC$_f$ fuel injection timings used in this study. Note that the figure does not represent the piston position at 220 °CA bTDC$_f$ (which is lower in the bore, promoting more wall impingement); the figure provides a visualization of the fuel-wall impingement concept and is for illustration purposes only.

2.6. Fuels

Eight fuels—six test and two control—were used in this study. Three of the test fuels were E10 fuels, and the other three were E25 fuels. Each ethanol grouping (i.e., E10 and E25) had fuels with RVPs of 8, 12, and 16 psi. The two control fuels were both E10 fuels with an RVP of 6.6 or 7.1 psi. All fuels were procured from Gage Products, with no detergent packages added to the fuels. Despite there being no detergent packages added to the fuels the day–to–day baselines, engine control setpoints, and measured emissions were very consistent though both the low and high load portions of the test, suggesting fuel injector depot effects could be minimal.

The properties of the test fuels varied in ethanol content and RVP. Within this range of properties, the associated fuel distillation varied, as shown in Fig. 5, which illustrates ASTM D86 data from the certificate of analysis provided by Gage Products, along with RD 587 and PACE 20, the two control fuels that were surrogates for E10. RD 587 is a full boiling range E10 surrogate, and PACE 20 is a nine-component surrogate. Additional details for both fuels can be found in Wagnon (2020) [59].

To better highlight the variations in the fuels, the ASTM D7096 simulated distillation of the fuels was also measured, including a modification to the ASTM D7096 protocol that added an effective and thorough cleaning procedure between samples. Splitter, et al. (2023) [60] provides detailed information about the approach [61] and rationale. The procedure is intended to measure the distillation curves of gasoline and gasoline–ethanol blends with a boiling point range within that of nC_3–nC_{16} hydrocarbons. This method further specifies analytical conditions established in ASTM D7096 to increase interlaboratory analytical precision. In this method, a wide-bore, nonpolar gas chromatography column is used to separate gasoline samples according to boiling point. Retention times and response factors of a calibration sample are used to calculate the volume percentage eluted at a given time—and by extension, the boiling point. Cumulative volume percentage and boiling temperature are plotted to yield a distillation curve. The associated findings for the fuels in this study are presented in Fig. 6 and are categorized by the ethanol content and RVP of the fuels.

Fuel properties beyond distillation were measured using ASTM test methods by Gage Products in the certificate of analysis in all cases except where noted; fuel properties are shown in Table 2. Published ASTM methods were used in all cases except for heat of vaporization (HoV); those results are presented in the appendix of Splitter, et al. (2023) [60].

2.7. Fuel spray measurements

Fuel spray measurements were performed in a pressure and temperature controlled constant volume spray vessel external of the engine, at fuel temperatures of 20, 40, and 75 °C, with ambient pressures of 40 and 200 kPa$_a$ and fuel injection pressures of 50 and 200 bar. Note, the spray vessel conditions effectively encapsulate the range of conditions used in the engine work where the fuel temperature was allowed to float between ambient (around 40 °C in the test cell) to up to the coolant temperature of 75 °C, intake manifold pressures of between 55 and 205 kPa$_a$, and fuel rail pressure of 100 bar. The injected mass was 10 and 15 mg for the 50 and 200 bar fuel injection pressures, respectively. Fuel spray images were acquired at 20 kHz with diffuse back illumination with a field of view of 120 mm. Penetration curves from five individual spray events were averaged for each operating condition. Spray patternation measurements of each fuel and condition were conducted at 40 mm from the injector tip. Sauter Mean Diameter (SMD) measurement of each spray were conducted at 40 mm from the injector tip.

3. Results

Results are divided into two main sections: Steady-State Engine Operation Results, and Unsteady Engine Operation Results. The first main section has 4 subsections, and the second main section has 4 subsections.

Table 2
Measured fuel properties for fuels used in this study.

Sample	Test Method	Units	PACE 20	RD 587	Tier III regular E10 RVP 8 psi	Tier III regular E25 RVP 8 psi	Tier III regular E10 RVP 12 psi	Tier III regular E25 RVP 12 psi	Tier III regular E10 RVP 16 psi	Tier III regular E25 RVP 16 psi
Specific gravity at 15.56 °C	ASTM D4052		0.7458	0.7484	0.7494	0.7560	0.7449	0.7492	0.7230	0.7320
Density at 15.56 °C	ASTM D4052	g/cc	0.7465	.7480	0.7487	0.7553	0.7440	0.7485	0.7223	0.7312
Ethanol content	ASTM D4815	vol %	9.49	9.93	10.14	24.98	9.72	25.16	10.02	25.35
Sulfur content	ASTM D 5453	wt %	0.0000	.00036	0.0007	0.0007	0.0008	0.0007	0.0006	0.0005
RVP at 100°F	ASTM D5191	psi (kPa)	6.6(45.5)	7.1(48.9)	8.0 (55.1)	7.9 (54.4)	11.8 (81.3)	12.3 (84.7)	16.7 (115.1)	16.1 (110.9)
PMI	ASTM D6730 Annex A1	-	1.584	1.818	2.118	1.845	2.214	1.870	1.903	1.303
D86 distillation	ASTM D86		Evaporated	Evaporated	Evaporated	Evaporated	Evaporated	Evaporated	Evaporated	Evaporated
Distillation, initial boiling point	ASTM D86	°C (°F)	43.2(109.8)	41.2(106.2)	38.3 (100.9	38.7 (101.7)	29.7 (85.5)	29.5 (85.1)	25.2 (77.4)	23.9 (75.0)
Distillation, 5 %	ASTM D86	°C (°F)	55.3(131.5)	54.9(130.8)	53.4 (128.1)	54.3 (129.7)	40.9 (105.6)	41.3 (106.3)	31.2 (88.2)	31.6 (88.9)
Distillation, 10 %	ASTM D86	°C (°F)	56.8(134.2)	57.6(135.7)	57.0 (134.6)	58.5 (137.3)	47.6 (117.7)	48.6 (119.5)	37.6 (99.7)	38.4 (101.1)
Distillation, 20 %	ASTM D86	°C (°F)	59.5(139.1)	61.1(142.0)	61.7 (143.1)	63.8 (146.8)	56.3 (133.3)	58.2 (136.8)	45.9 (114.6)	47.8 (118.0)
Distillation, 30 %	ASTM D86	°C (°F)	61.9(143.4)	64.4(147.9)	65.5 (149.9)	67.9 (154.2)	62.5 (144.5)	64.8 (148.6)	53.5 (128.3)	56.5 (133.7)
Distillation, 40 %	ASTM D86	°C (°F)	67.9(154.2)	70.8(159.4)	72.6 (162.7)	70.9 (159.6)	66.8 (152.2)	69.5 (157.1)	60.4 (140.7)	64.6 (148.3)
Distillation, 50 %	ASTM D86	°C (°F)	89.7(193.5)	98.0(208.4)	99.2 (210.6)	73.3 (163.9)	85.0 (185.0)	72.9 (163.2)	66.4 (151.5)	70.9 (159.6)
Distillation, 60 %	ASTM D86	°C (°F)	100.2 (212.4)	113.8 (236.8)	113.6 (236.5)	75.2 (167.4)	113.8 (236.8)	75.1 (167.2)	86.9 (188.4)	74.6 (166.3)
Distillation, 70 %	ASTM D86	°C (°F)	107.0 (224.6)	125.8 (258.4)	124.7 (256.5)	114.7 (238.5)	128.9 (264.0)	79.0 (174.2)	120.3 (248.5)	76.7 (170.1)
Distillation, 80 %	ASTM D86	°C (°F)	117.3 (243.1)	139.5 (283.1)	139.5 (283.1)	134.6 (274.3)	142.7 (288.9)	135.0 (275.0)	137.1 (278.8)	123.7 (254.7)
Distillation, 90 %	ASTM D86	°C (°F)	165.9 (330.6)	157.6 (315.7)	159.6 (319.3)	155.4 (311.7)	161.7 (323.1)	154.5 (310.1)	156.1 (313.0)	149.6 (301.3)
Distillation, 95 %	ASTM D86	°C (°F)	174.9 (346.8)	171.4 (340.5)	178.1 (352.6)	172.8 (343.0)	180.5 (356.9)	173.3 (343.9)	176.2 (349.2)	169.9 (337.8)
Distillation, dry point	ASTM D86	°C (°F)	189.9 (373.8)	205.1 (401.2)	210.9 (411.6)	210.0 (410.0)	213.6 (416.5)	209.2 (408.6)	211.1 (412.0)	207.1 (404.8)
Recovery	ASTM D86	vol %	98.5	98.3	98.1	98.1	97.0	96.9	96.0	96.4
Residue	ASTM D86	vol %	1.1	1.0	1.0	1.0	1.1	1.1	1.1	1.1
Loss	ASTM D86	vol %	0.4	0.7	0.9	0.9	1.9	2.0	2.9	2.5
Net heat of combustion	ASTM D240	MJ/kg (Btu/lb)	41,87 (18,000.86)	42.27 (18,172.83)	41.80 (17,970.77)	39.00 (16,766.98)	41.71 (17,932.07)	39.20 (16,852.97)	41.97 (18,043.85)	38.73 (16,650.90)
Carbon content	ASTM D5291	wt %	82.90	82.79	82.82	77.08	82.68	77.11	82.36	76.52
Hydrogen content	ASTM D5291	wt %	13.60	13.54	13.44	13.82	13.72	13.64	13.84	13.95
Oxygen content	ASTM D5291	wt %	3.50	3.66	Not tested	9.10	3.60	9.25	3.80	9.53
C/H ratio	Calculated ASTM D5291	wt/wt	6.097	6.114	6.162	5.577	6.025	5.653	5.951	5.485
H/C ratio	Calculated ASTM D5291	mol/mol	1.955	1.949	1.934	2.137	1.978	2.108	2.003	2.173
O/C ratio	Calculated ASTM D5291	mol/mol	0.032	0.033	0.034	0.089	0.033	0.090	0.035	0.093
Heat of vaporization at 10 °C	NREL in-house method	kJ/kg	–	–	400.9	539.8	423.0	540.5	412.9	565.5

(*continued on next page*)

Table 2 (*continued*)

Sample	Test Method	Units	PACE 20	RD 587	Tier III regular E10 RVP 8 psi	Tier III regular E25 RVP 8 psi	Tier III regular E10 RVP 12 psi	Tier III regular E25 RVP 12 psi	Tier III regular E10 RVP 16 psi	Tier III regular E25 RVP 16 psi
Density at 0 °C	ASTM D4052 mod	g/cm^3	–	–	0.7615	0.7698	0.7582	0.7628	0.7369	0.7456
Density at 10 °C	ASTM D4052 mod	g/cm^3	–	–	0.7527	0.7613	0.7494	0.7541	0.7277*	0.7366*
Density at 20 °C	ASTM D4052 mod	g/cm^3	–	–	0.7437	0.7522	0.7397*	0.7455*	0.7186*	0.7238*
Surface tension at −10 °C	ASTM D1331 mod	mN/m	–	–	23.086	23.172	22.925	22.694	21.691	21.698
Surface tension at 0 °C	ASTM D1331 mod	mN/m	–	–	22.546	22.615	22.266	22.116	21.076	21.047
Surface tension at 10 °C	ASTM D1331 mod	mN/m	–	–	21.799	21.774	21.520	21.370	20.320	20.360
Surface tension at 20 °C	ASTM D7042 mod	mN/m	–	–	21.077	21.107	20.860	20.645	**	**

* A stable measurement could not be established because of bubble formation in the cell from light components. The given data are the last readings before bubble formation was recorded.

** Measurements could not be made at this temperature because of fuel volatility.

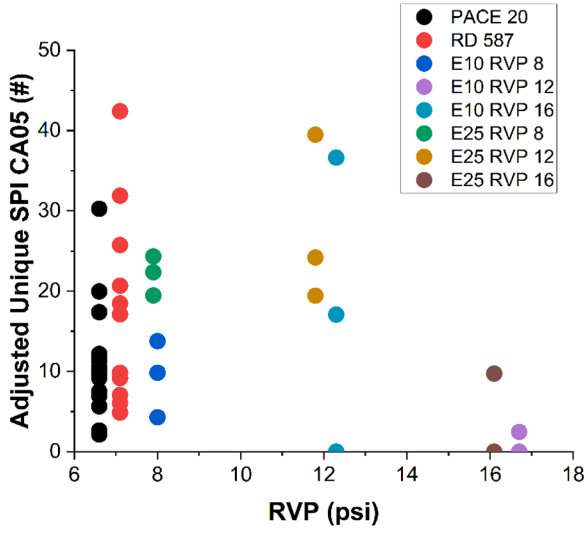

Fig. 7. The adjusted unique SPI count as a function of fuel RVP indicates a complex relationship between RVP and SPI event totals.

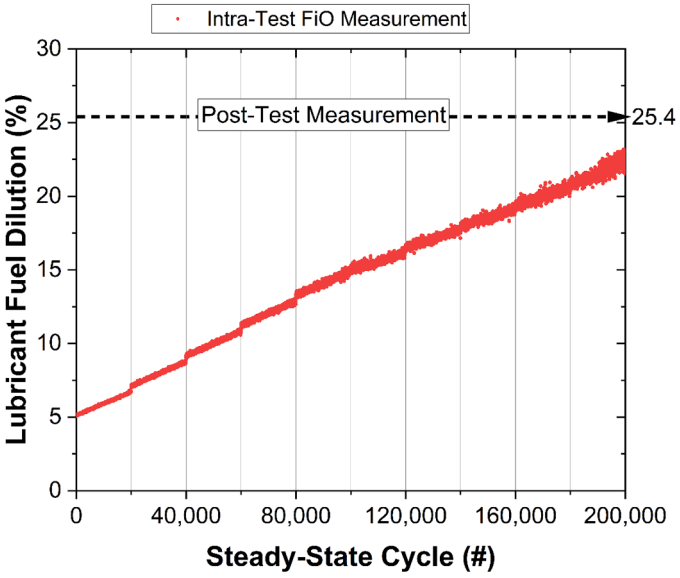

Fig. 8. The RD 587 FiO-based measurement of fuel dilution is plotted as a function of steady-state cycle (red), and the physical post-test measurement of lubricant fuel dilution (dashed line) is shown at 25.4 %.

3.1. Steady-state engine operation results

3.1.1. Fuel-wall impingement at steady-state engine operation

Analyzing the adjusted unique SPI as a function of RVP (Fig. 7) showed no direct correlation but instead suggested a complex relationship between RVP and SPI event totals. Specifically, RVP at or below 8 psi resulted in little to no direct effect on SPI. For RVP of 12 psi, a wide variability in SPI with the highest average unique SPI count for a given fuel was observed. At RVP of 16 psi, the unique SPI count approached zero. This relationship was not anticipated, so further analysis was performed on the sources of this initial observation.

Because the experimental approach used the online FiO measurement of lubricant fuel dilution, understanding whether a correlation exists between fuel impingement and lubricant fuel dilution is important. The approach to determine lubricant fuel dilution is relatively straightforward. Both the online fuel dilution measurement [24] and physical weighing of the lubricant mass were performed before and after each test. The comparison of the two approaches is shown in Fig. 8, where the online FiO measurement (red data) is plotted as a function of the steady-state test cycle. The vertical divisions in the plot indicate each of the 10 segments in the test sequence. The dashed horizontal line at 25.4 % is the post-test fuel dilution measured by physically draining and weighing the oil on a scale before and after the test sequence. The data in Fig. 8 show that both measurement methods achieved similar values by the end of the test. Additionally, the good overall agreement of both methods and the high lubricant fuel dilution value at the end of the 300 min test highlight that retarded fuel injection timing (−220 °CA aTDC$_f$) and the reduced coolant and lubricant temperatures (75 °C) used in the test sequence achieved quite high lubricant fuel dilution levels. Note that the dry-sump modification of the engine increased the total lubricant volume to approximately 2 gal, resulting in an average over 42 tests of 6562 ± 61 g lubricant filled per test.

Results in Fig. 8 also indicate that the FiO measurement data have an initial offset error of approximately 5 % despite the triple flush of lubricant used after each test. This small offset in the data suggests that a lower noise floor could exist in the FiO approach. Furthermore, Fig. 8 shows that the FiO measurement captures the segment-to-segment steps through the initial segments, and then the data become less deterministic. This temporal evolution is attributed to signal saturation, particulate matter, and aeration effects in the lubricant, as shown by prior work [23,24].

Despite these minor discrepancies, the information from the FiO

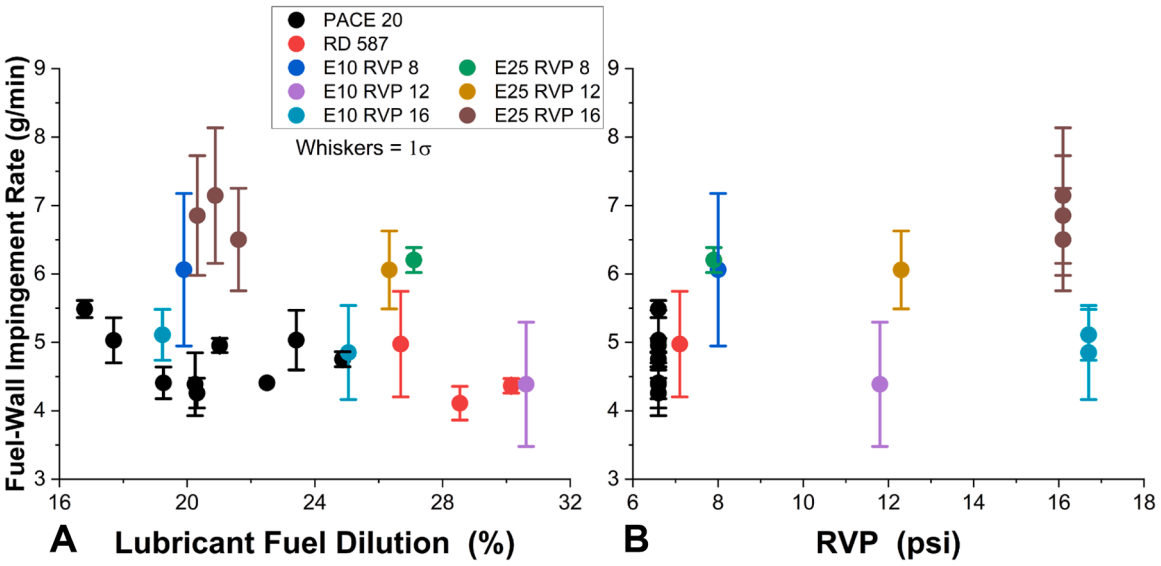

Fig. 9. The FWI rate for each fuel is plotted as a function of fuel lubricant dilution (A) and RVP (B).

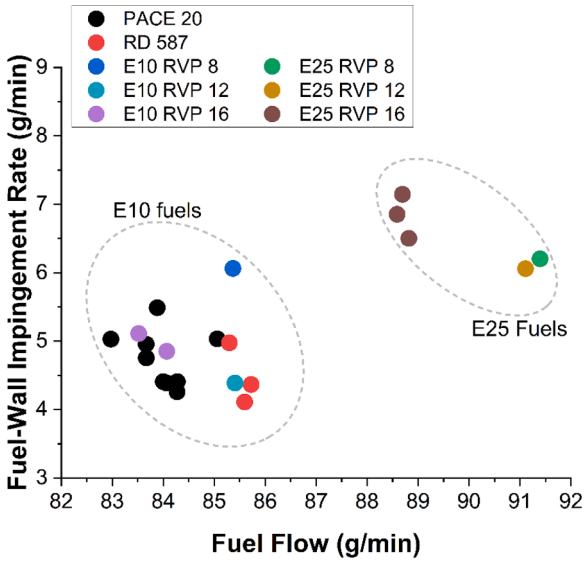

Fig. 10. The fuel-wall impingement rate is shown as a function of fuel flow rate, and the colors of the circles indicate the fuel ethanol content.

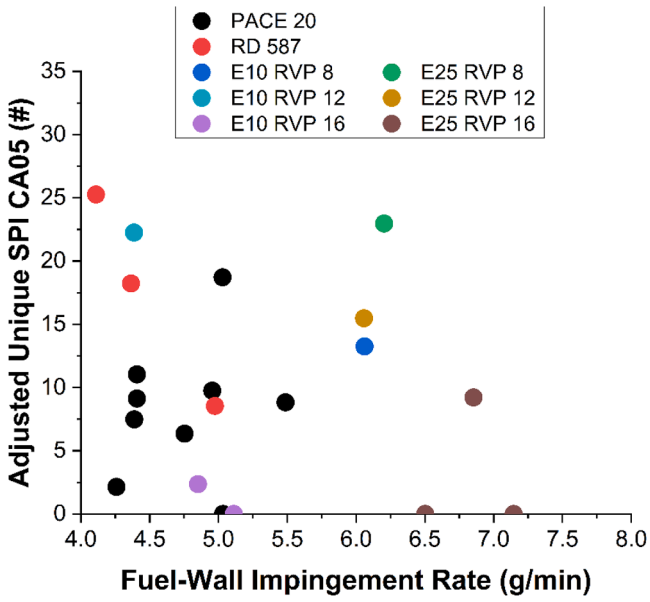

Fig. 11. Unique SPI events for each fuel are shown as a function of fuel-wall impingement rate.

diagnostic affords the calculation of fuel-wall impingement rate, which was calculated for each fuel using the following approach. Based on the FiO temporal evolution throughout the test, a discretization of the data for the first six segments was used to analyze each segment independently with the slope of the FiO in a respective segment determined. Then, the average FiO rate for the test was calculated based on the first six segments. The approach is outlined in Eqs. (2),(3), where $Mass_{Oil,\ i=0}$ is the initial mass of oil before the test, $FiO_{@\ start,i}$ is the FiO measurement at the start of segment i, t_i is the time in segment i, and $FiO_{slope,i}$ is the slope of the FiO in segment i via linear fit. Because only the first 6 segments (of the 10 segments in each test) were used in the determination of fuel-wall impingement, only those 6 segments were used in the calculation (i.e., in Eq. (3), $n = 6$ and not 10) of the fuel-wall impingement rate (FWI).

$$FiO\ mass_i = \frac{Mass_{Oil,\ i=0} \times \left[1 + \left\{FiO_{@\ start,i} + \left(t_i \times FiO_{slope,i}\right)\right\}\right]}{100} \quad (2)$$

$$FWI = \sigma\left[\sum_{1}^{n} \frac{d\left(FiO\ mass_i - Mass_{Oil,\ i=0}\right)_t}{t_i}\right] \quad (3)$$

The resulting fuel-wall impingement rate for each fuel is plotted as a function of RVP in Fig. 9A and 9B Interestingly, results in Fig. 9A indicate that there is no direct relationship between fuel-wall impingement and lubricant fuel dilution. Moreover, for a given lubricant dilution (e.g., 20 %), multiple fuel-wall impingement values—which appear to be somewhat grouped by ethanol level—can occur. Specifically, apart from the E10 RVP 8 fuel, the E25 fuels exhibit slightly increased fuel-wall impingement rates. The color coding of Fig. 9A is echoed and reinforced more directly in Fig. 9B, which in general shows no direct correlation of fuel RVP with fuel-wall impingement in the steady-state portion of the test examined here. However, the E25 fuels exhibited an approximate 1 g/min increase compared with that of the E10 fuels. Note that whiskers in Fig. 9 are the calculated fuel wall impingement standard

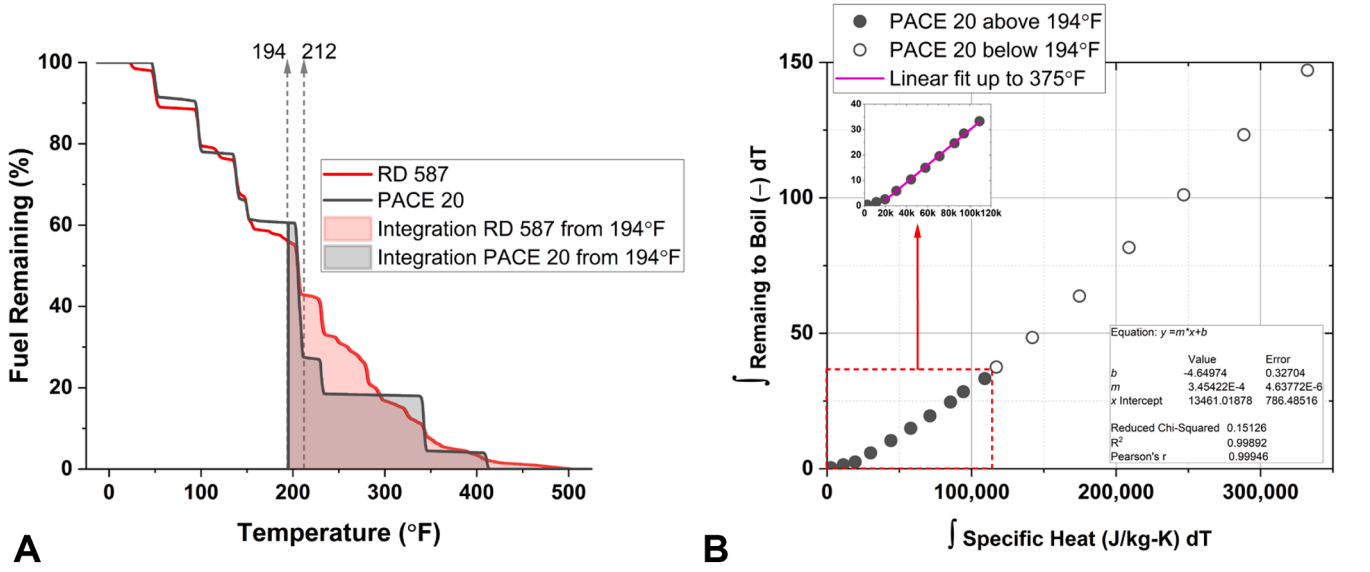

Fig. 12. The charts illustrate the approach used to determine fuel remaining to boil (A) and the physical–chemical thermodynamic-based meaning of fuel remaining to boil (B).

deviation within each run, and the marker denotes the respective mean. The increase in fuel-wall impingement rate with the E25 fuels is more directly apparent in Fig. 10, which plots it as a function of fuel flow rate. Although the fuel flow with E25 is higher because of the reduced energy density of ethanol, the fuel-wall impingement rate does not have a 1-to-1 relation with fuel flow. Whereas the E25 fuels required approximately 6 g/min higher fuel flow, the fuel-wall impingement rate only increased by approximately 1 g/min with these fuels. This means that with E25 relative to E10 fueling the measured increase in fuel wall impingement is not a 1-to-1 relation with the increase in fuel mass needed to conserve fuel energy. A similar observation by this research team was reported in prior work [42], which showed E25 fuels relative to E0 fuels exhibited less than a 1-to-1 increase in fuel wall impingement relative to the increase in fuel mass required for energy neutrality.

Although Fig. 10 shows an increased fuel-wall impingement rate with the E25 fuels, results in Fig. 11 show that fuel-wall impingement has no effect on unique SPI events regardless of ethanol content or RVP. In fact, an inverse correlation could be more likely because increased fuel-wall impingement cases tended to have reduced unique SPI totals. This observation is somewhat counterintuitive because one of the working hypotheses of SPI is that fuel-wall impingement suggests that an opportunity to create *An spi* source term exists. Thus, the lack of SPI dependency clearly demonstrates that SPI is not a function of the fuel merely impinging on the cylinder liner, and additional factors must also be considered. Note that a prior study [42] suggested similar findings in E0 and E25 fuels but did not explore RVP or unsteady operation effects. To further investigate the source of this inconsistency, the present work explored the effect of fuel properties on the impinged fuel to ascertain fuel effects on which SPI in steady-state operation could be dependent.

3.1.2. Steady-state engine operation fuel retention effects on SPI

The findings in Fig. 11 motivated an alternative approach to determine fuel retention. This approach—which calculates the integral of the ASTM 7096 simulated distillation for each fuel above the suspected liner temperature to the final fuel distillation temperature [60,62]—is described in detail in Splitter, et al. (2023) [60]. Fig. 12A depicts the results of this approach for PACE 20 and RD 587 fuels, showing the integration of the fuel remaining to boil above the suspected liner temperature when the integration was performed from 194°F to 212°F (90 °C and 100 °C, respectively); this was the range of the assumed liner temperature up to the final boiling point of the fuel based on the complex conjugate heat transfer results from Mills et al. [63]. for this engine. The integration was performed from above the assumed liner temperature because the assumption is that the fuel evaporation below the liner temperature is not rate-limited; thus, fuel species with boiling points below the liner temperature fully evaporate.

Results of this framework indicate that a larger remaining-to-boil integral means that more energy is needed to evaporate the fuel (i.e., more fuel would be retained). Conversely, a smaller remaining-to-boil integral means less energy is needed to evaporate the fuel (i.e., less fuel would be retained). Note that Mayer et al. performed a similar approach [21], but that work used ASTM D86 integrated data from 150 °C with no adjustment for ethanol content. The present work has found the ASTM D86 approach to be less accurate than the ASTM 7096 approach in low- and high-temperature ranges of the distillation curve, and the work by Mills et al. [63]. has shown that the liner temperature is closer to the coolant temperature independent of engine load. Additionally, Splitter, et al. (2023) [60] showed that an HoV adjustment for the integration temperature was needed for varying ethanol content to normalize data to the effect of a common ethanol level.

Results of the integration process for PACE 20 depicted in Fig. 12A are then plotted as a function of the integrated specific heat of fuel species in PACE 20, up to the fuel species respective boiling point in Fig. 12B The results in Fig. 12B highlight that the integration of the inverted ASTM 7096 distillation curve from above the liner temperature to the final boiling temperature is directly proportional to the energy required to raise the temperature of the fuel. This approach assumes that as fuel species reach the boiling point, they are no longer considered in the specific heat integration and that pressure has no effect on the process. Note that the units of the integration process are %-°F, which become non-physical, and thus the integration units are omitted in the subsequent discussion and the integrated value stands for more of a representative empiricism with the energy to evaporate the fuel as highlighted through the relationship in Fig. 12B

Using this approach, the fuel remaining to boil for each of the fuels in this study was calculated. For the E25 fuels, a secondary adjustment for fuel HoV was undertaken to normalize the effects of HoV to an E10 basis (i.e., adjust 25 % ethanol results to a 10 % ethanol basis). The adjustment assumed that increased ethanol content increases charge cooling and thus reduces liner temperature and starting integration temperature of the ASTM 7096 data for the E25 fuels. Specifically, for 25 % ethanol vs. 10 % ethanol at this study's operating conditions and fueling rates, a

Table 3
The fuel remaining to boil for each test fuel of this study is shown with starting temperature ranges of integration processes, average, and spread of the starting temperature approaches noted.

Fuel	Remaining to boil above 212°F (–)	Remaining to boil above 194°F (–)	Remaining to boil above 189°F (–)	Remaining to boil above 171°F (–)	Average (–)	Spread (–)
PACE 20	28.43	36.92	—	—	32.67	8.49
RD 587	37.02	46.15	—	—	41.58	9.13
E10 RVP 8	37.02	45.59	—	—	41.31	8.57
E10 RVP 12	41.33	49.45	—	—	45.39	8.12
E10 RVP 16	35.52	42.44	—	—	38.98	6.92
E25 RVP 8	—	—	38.92	48.05	43.49	9.13
E25 RVP 12	—	—	36.06	43.82	39.95	7.74
E25 RVP 16	—	—	31.61	38.18	34.90	6.57

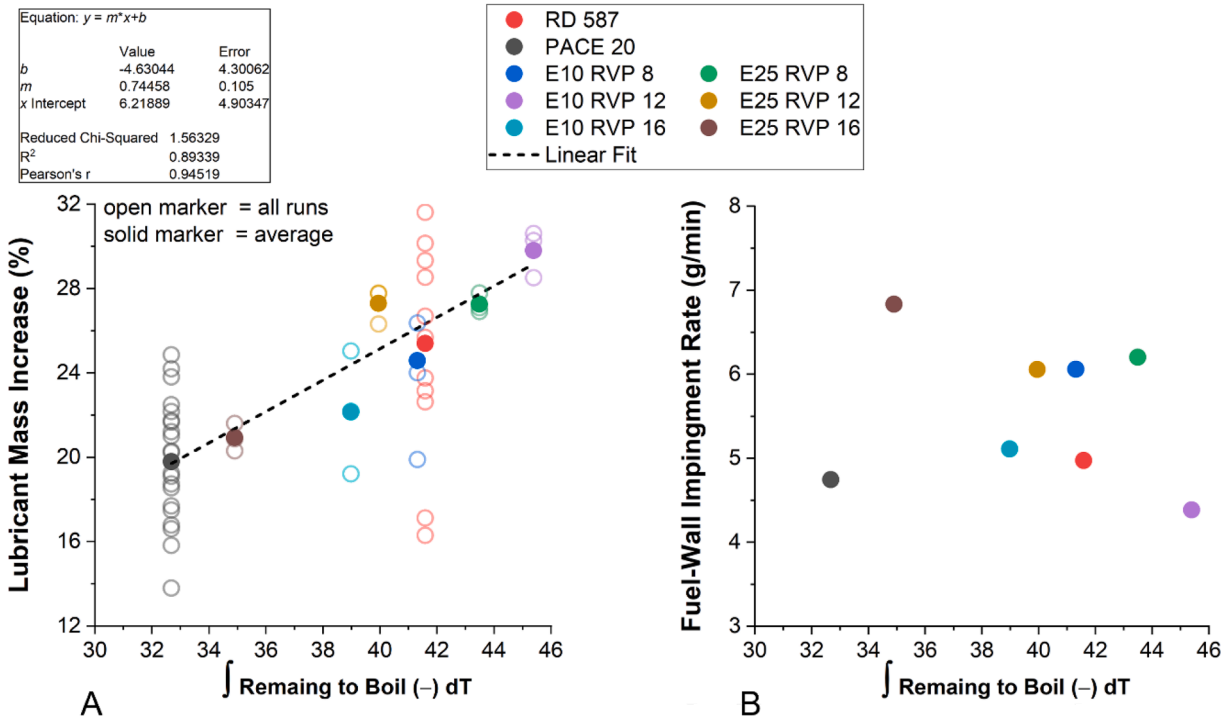

Fig. 13. The lubricant mass increase from physical scale-based measurements is plotted as a function of fuel remaining to boil (A), and the fuel wall impingement rate from the FiO diagnostic is plotted as fuel remaining to boil (B).

13 K reduction in-cylinder temperature is calculated assuming complete vaporization at the time of injection. Thus, for the E25 fuels, the integration of the simulated distillation ASTM 7096 data started at a 13 K lower temperature than that of the E10 fuels (189°F and 171°F for the E25 fuels vs. 212°F and 194°F for the E10 fuels, respectively). Further details on this adjustment are outlined with supporting calculations in Splitter, et al. (2023) [60]. The resulting integration data—temperatures used in the integration, average, and spread of the integration—are presented in Table 3.

Using the combined simulated distillation integration values in Table 3, the lubricant mass increase and fuel-wall impingement rates were plotted as a function of the fuel remaining to boil in Fig. 13A and 13B, respectively. From the results, the lubricant mass increase from fuel dilution was highly linear for the fuel remaining to boil, with an R-squared value of nearly 0.85. Note the whiskers in the x direction in Fig. 13A (and 13 B) are the data spread from the integration process, a result of the two different assumed temperatures (i.e., 212°F and 194°F for the E10 fuels, and 189°F and 171°F for the E25). The y-axis whiskers are the spread in the measurement of the sump mass increase (Fig. 13A) or the calculated fuel-wall impingement rate (Fig. 13B). In each figure, the markers are the average of the respective fuel and approach.

Interestingly, the general trends in Fig. 13A and 13B are inverted. That is, increasing the fuel remaining to boil (i.e., a fuel that takes more energy to boil above the liner temperature) increases the lubricant mass increase over the test and therefore increases fuel dilution of the lubricant. Conversely, increasing the fuel remaining to boil appears to decrease the fuel-wall impingement rate. What can be gleaned from this counterintuitive result is that this relationship can occur only if the fuels requiring more energy to evaporate impinge less, yet the effect of their impingement is more significant.

To further elucidate this complex relationship between fuel impingement and associated fuel retention, the measured engine carbon balance was calculated using the measured fuel flow and airflow rates. For all fuels and tests, the exhaust lambda (λ_{exh}) of stoichiometry (i.e., $\lambda_{exh} = 1$) was maintained as measured by exhaust gas oxygen and emissions bench measurements and a wideband oxygen sensor. Although $\lambda_{exh} = 1$ was maintained, the fueling provided to the engine was allowed to float as needed to achieve $\lambda_{exh} = 1$. For all tests, the high

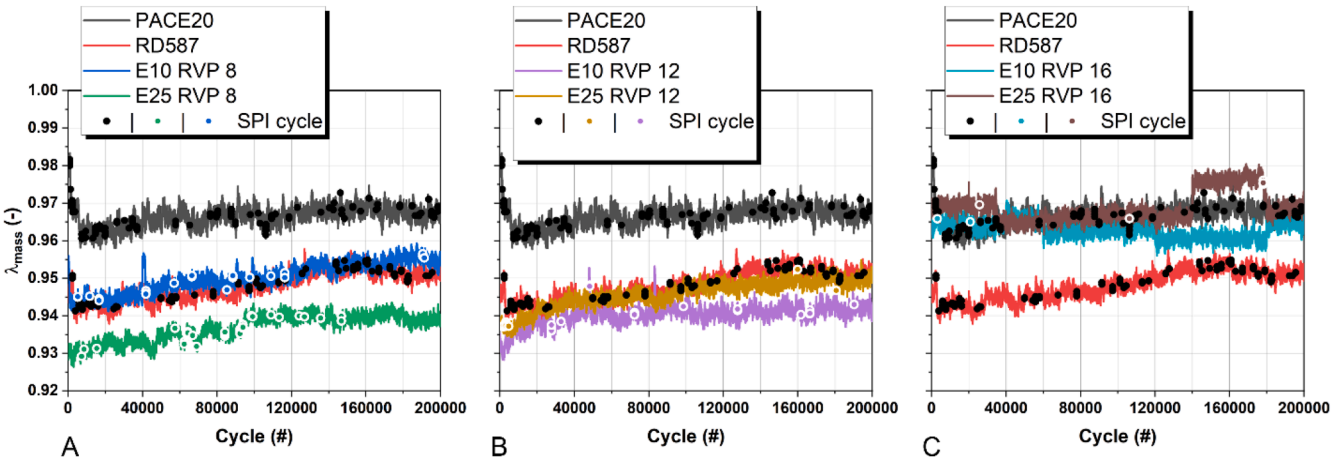

Fig. 14. λ_{mass} plotted as a function of a steady-state test cycle for RVP 8 fuels (A), for RVP 12 fuels (B), and for RVP 16 fuels (C), with PACE 20 and RD 587 control fuels plotted for reference in each figure. SPI events denoted as color matching open circles for test fuels and closed black markers for PACE 20 and RD587.

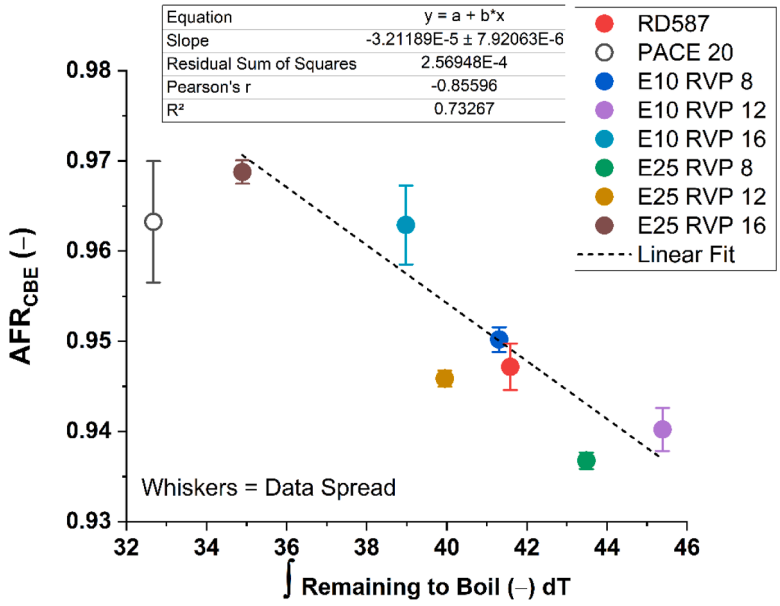

Fig. 15. The carbon balance error is shown with respect to fuel remaining to boil with linear fit added.

rate of fuel-wall impingement required the actual fueling rate to the engine to be higher than that required to meet stoichiometric exhaust, meaning that excess fueling was needed because of fuel retention and associated lubricant fuel dilution in the engine. The average of the lambda of the supplied fuel/air to the engine (λ_{mass}) from all tests is plotted as a function of a steady-state test cycle in Fig. 14A for RVP 8 fuels, Fig. 14B for RVP 12 fuels, and Fig. 14C for RVP 16 fuels. In each figure, control fuels PACE 20 and RD 587 are also plotted for reference.

The average λ_{mass} for each fuel grouped by RVP and relative to the control fuels is plotted in Fig. 14. For each fuel, the average was calculated as the average of a back-to-back-to-back triplicate of the data. The average was used because the λ_{mass} can change following large SPI events; the averaging was used to help prevent bias from a single run. Fig. 14 highlights several facts. The first is that for all fuels, as the test progressed, the λ_{mass} tended to numerically increase (i.e., the carbon balance error was reducing over the test). Secondly, Fig. 14A shows that the λ_{mass} of E10 RVP 8 and RD 587 are very similar, whereas E25 RVP 8 has a reduced λ_{mass} (i.e., the carbon balance error is larger). Fig. 14B shows that both RVP 12 test fuels are most similar to RD 587—with E10 RVP 12 having a slightly reduced λ_{mass} of the two RVP 12 fuels—a profile similar to that of E25 RVP 8. Last, both RVP 16 fuels exhibited λ_{mass} like PACE 20, with significant variation and volatility in the λ_{mass} over the test duration, and with the least defined long-term reduced λ_{mass} structure over the test.

Although Fig. 14 provides valuable information and long-term structures that could exist in λ_{mass}, a more direct comparison of the results is desirable. To distill the trend in λ_{mass} from Fig. 14 down to an single average value for each fuel, the average carbon balance error (AFR_{CBE}) of the engine was calculated using Eq. (4) on a segment-by-segment basis. The airflow supplied to the engine in segment i is $flow_{air,i}$, the fuel flow to the engine in segment i is $flow_{fuel,i}$, AFR_{stoich} is the stoichiometric AFR for each fuel, and σ is the mean of all calculations on a segment-by-segment basis. Thus, if $AFR_{CBE} = 1$, then no excess fueling is needed to meet $\lambda_{exh} = 1$ (i.e., the carbon input into the engine matches the carbon measured in the exhaust manifold). However, because of the retarded injection timing and high load and fueling rates used in this study, all of the fuels exhibited $AFR_{CBE} < 1$ for all experiments (Fig. 15), signifying that more carbon (i.e., fuel) was supplied to the engine than was measured in the exhaust (e.g., some of the injected fuel was lost to the oil sump and was not burned or expelled).

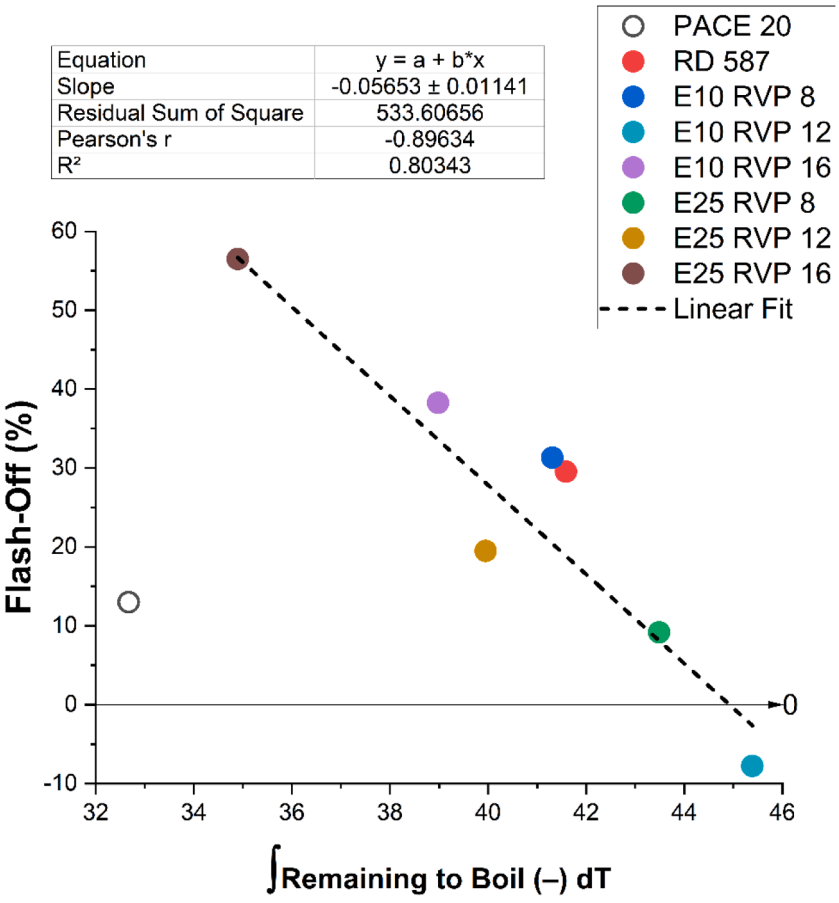

Fig. 16. Calculated fuel flash-off is plotted as a function of fuel remaining to boil above the liner temperature.

$$AFR_{CBE} = \sigma_{i=1}^{i=n}\left[flow_{fuel,i} \times \left(1 - \frac{\left(\frac{flow_{air,i}}{flow_{fuel,i}}\right)}{AFR_{stoich}}\right)\right] \quad (4)$$

The AFR_{CBE} trend in Fig. 15 shows a linear dependency on carbon balance error with respect to the calculated fuel remaining to boil, meaning that the engine overfueling amount increases (i.e., AFR_{CBE} numerically decreases) as a function of increasing a fuel's integrated remaining to boil property. The data markers are the overall average of each fuel, and the whiskers are the data spread of the different segments of the test. Note that the only significant deviation from this trend is the result for PACE 20, the nine-component surrogate fuel. PACE 20 has an unusual distillation behavior near the liner temperature because 34.04 % of the fuel boils at this temperature (209°F or 210°F for the 10.63 % n-heptane or 23.41 % isooctane, respectively). Although mathematically accurate and notionally thermodynamically accurate, this high fuel fraction boiling at a common temperature skews the integration process somewhat relative to full boiling range fuels. Because of this, the data for PACE 20 were omitted from the linear fitting in Fig. 15 as well as Fig. 16, which is in Section 3.1.3.

The highly linear trend in AFR_{CBE} with respect to fuel remaining to boil suggests that as the energy needed to boil the fuel above the liner temperature increases, the overfueling needed to maintain $\lambda_{exh} = 1$ proportionally increases. Therefore, AFR_{CBE} could also indicate a potential source for SPI from fuel/lubricant interaction and films that could form SPI initiation sources. Furthermore, the AFR_{CBE} trend could hypothetically indicate increasing abnormal combustion through unfavorable or erratic local fuel stoichiometry at the ignition source. To determine the fate of excess fuel from AFR_{CBE}, the impinged fuel flash-off and associated fuel retention were calculated.

3.1.3. Steady-state engine operation fuel flash-off results

SubSection 3.1 highlighted that SPI was not correlated with fuel-wall impingement, but subSection 3.2 illustrated that AFR_{CBE} was found to correlate with fuel distillation (fuel remaining to boil). To determine if a positive interaction exists among fuel-wall impingement, AFR_{CBE}, and fuel remaining to boil, the fuel flash-off was calculated. Fuel flash-off is defined as the amount of the impinged fuel that evaporates from the liner. The approach used in this study is outlined in Eqs. (5) and (6), where the fuel mass error (FME) is calculated by the average of the excess fuel supplied in segment i ($flow_{fuel,i}$) and the average of the lambda in segment i ($\lambda_{mass,i}$). The associated flash-off is calculated by taking the percentage difference between the fuel-wall impingement (Eq. (3)) and the fuel mass error. Thus, this approach calculates the ratio of the impinged fuel minus the excess fueling that was needed in a segment as a function of the impinged fuel. A value of 100 would mean that all of the impinged fuel evaporated (no fuel retention, and thus FME = 0); a value of zero means that all of the impinged fuel was retained.

$$FME = \sigma\left[\sum_{1}^{n}\sigma(flow_{fuel,i}) \times (1 - \sigma(\lambda_{mass,i}))\right] \quad (5)$$

$$Flash - Off = 100 \times \frac{FWI - FME}{FWI} \quad (6)$$

The fuel mass error results for all fuels are presented in Fig. 16. Clearly, flash-off has a linear dependency on fuel remaining to boil (i.e., the integrated distillation area above the liner temperature). This is a logical finding because an increase in the integrated distillation results in more energy needed to evaporate the fuel, but the energy flux available for evaporation is finite.

Interestingly, the highest integrated distillation area above the liner

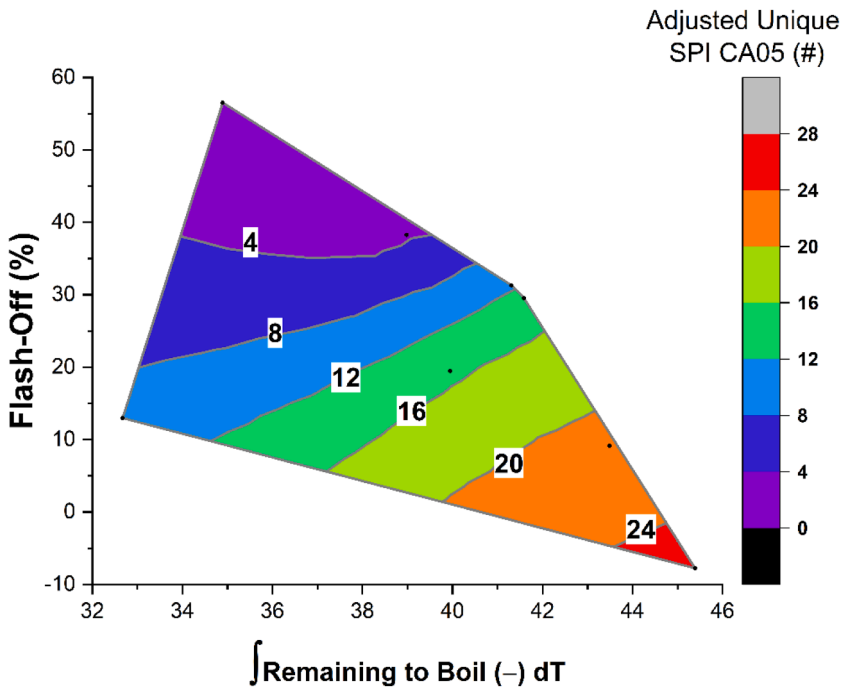

Fig. 17. Fuel flash-off is plotted as a function of fuel remaining to boil above the liner temperature with contours of unique SPI plotted on top.

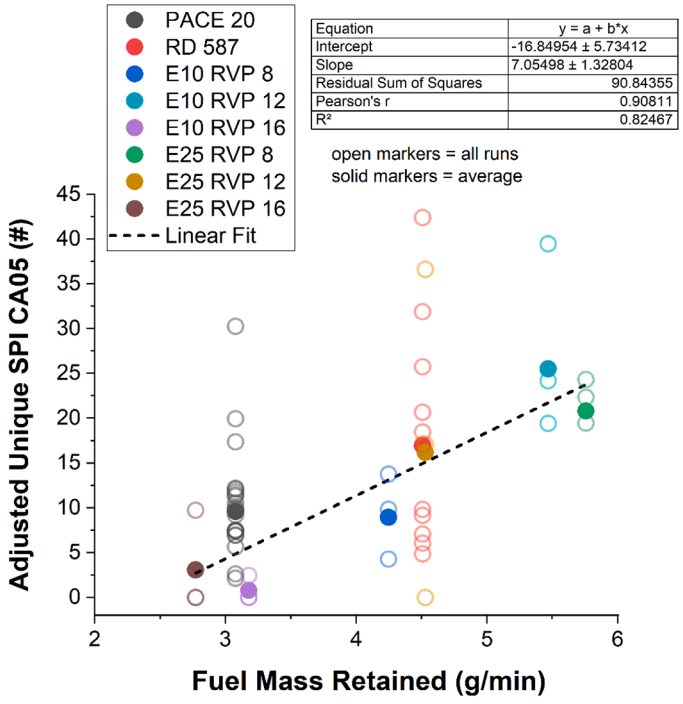

Fig. 18. Unique SPI is plotted as a function of fuel mass retained for all fuels.

temperature (E10 RVP 12) exhibits near zero flash-off; in fact, the flash-off is calculated to be slightly negative. The negative value is attributable to measurement errors in the calculation of *AFR* because the present work had *AFR* uncertainty within 1 % (shown in Fig. 15), which could cause up to a 10 % error in the flash-off calculation. This error applies across the range of measurements but is most pronounced in its effect in the lowest flash-off fuels. Results in Fig. 16 demonstrate that an impinged fuel's ability to flash off the liner is inversely proportional to the fuel distillation properties. Again, the present work is for a given operating condition and under the steady-state portion of the test sequence. Thus, results here could vary for different engine speeds, fueling rates, impingement masses, and coolant temperatures. However, these results highlight that for a given condition, fuel properties directly

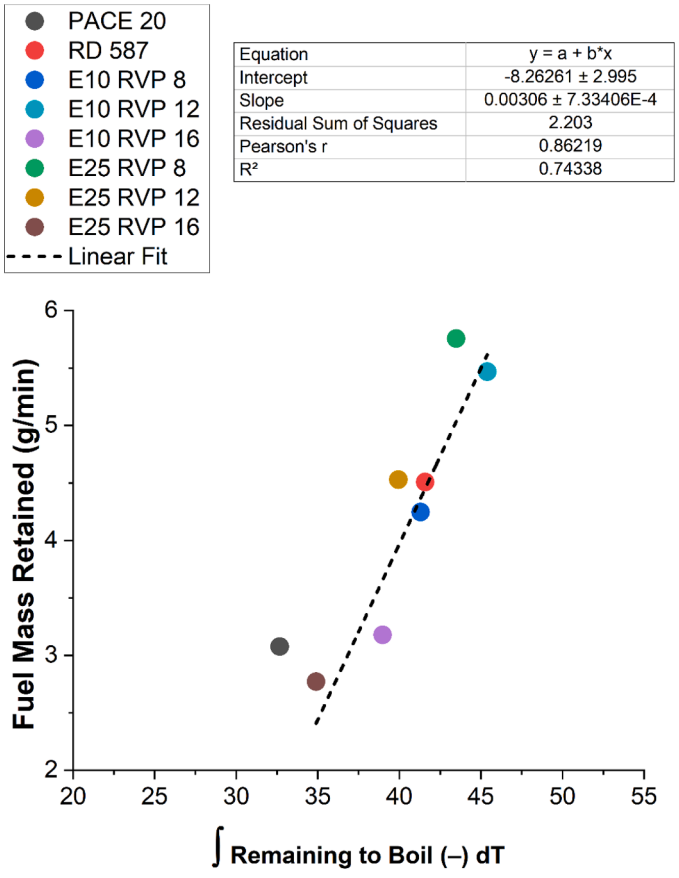

Fig. 19. Fuel mass retained is plotted as a function of fuel remaining to boil above the liner temperature for the select study fuels.

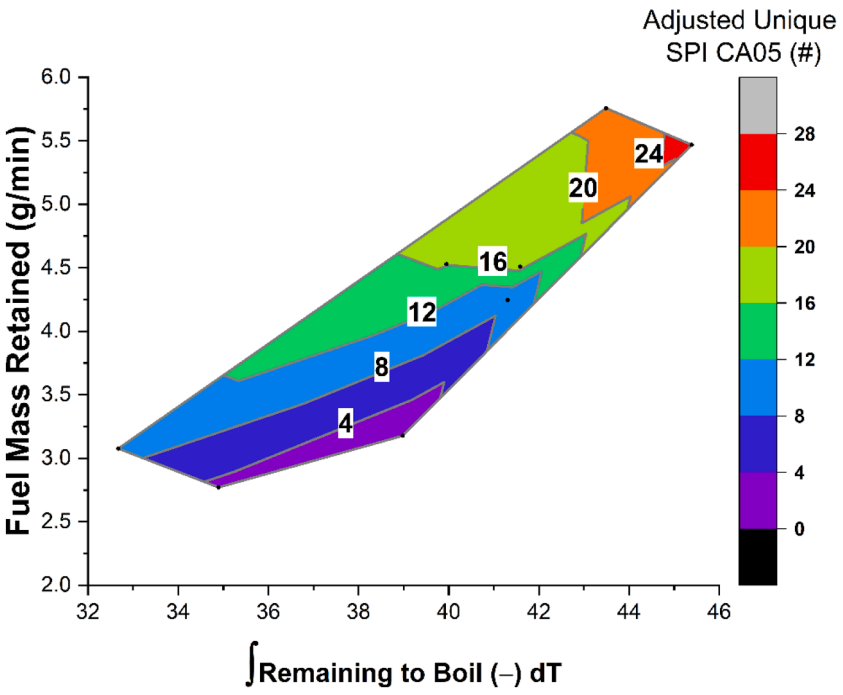

Fig. 20. Unique SPI contours are plotted as a function of FMR in the engine and fuel remaining to boil.

affect fuel flash-off.

Combining the flash-off, fuel remaining to boil, and SPI measurements yields the trend shown in Fig. 17. This multivariable analysis indicates that fuel flash-off decreases as the fuel remaining to boil increases and that the SPI propensity likewise increases (contour shading). This means that for impinged fuel, increasing the energy needed to evaporate above the liner temperature increases the SPI rate (i.e., as more fuel is retained on the cylinder liner, the SPI rates increase). This analysis is the focus of the next section of the present work.

3.1.4. *Steady-state engine operation fuel mass retained results*

Data in Fig. 17 highlight that SPI propensity is inversely proportional to fuel flash-off. The inverse of flash-off is correspondingly the fuel mass retained. The fuel mass retained (FMR) was calculated using Eq. (7), where $flow_{fuel,i}$ is the fuel flow in segment i, and $\lambda_{mass,i}$ is the lambda in segment i.

$$FMR = \sigma\left[\sum_{1}^{n} \sigma\left(flow_{fuel,i}\right) \times \left(1 - \sigma\left(\lambda_{mass,i}\right)\right)\right] \tag{7}$$

Unique SPI counts as a function of fuel mass retained are plotted in Fig. 18. Note the golden data (E25 RVP 12 psi) are more suspect because the adjustment for engine age (Fig. 2) was large under this condition owing to long engine life. The data indicate that the unique SPI is linearly dependent on fuel mass retained, highlighting that not only is impingement needed but, more importantly, fuel retention also is critical for SPI propensity. Although the linear trend has a reasonable fit for the acquired data, the intercept of the fit is nonphysical (i.e., at 0 fuel mass retained, the SPI count would be negative). Thus, the data suggest that SPI is dependent upon fuel mass retained, but a threshold minimum value was required to increase SPI, at least for the conditions, fuels, lubricants, and hardware explored in this study.

Likewise, the fuel mass retained is plotted as a function of the fuel remaining to boil (i.e., a fuel property) in Fig. 19. The data show that increasing the energy needed to evaporate the fuel above the liner temperature increases fuel mass retention.

Conflating the data in Figs. 18 and 19 allows the unique SPI to be plotted as contours as a function of fuel mass retained and fuel remaining to boil, as shown in Fig. 20. Using this approach, increasing the fuel remaining to boil increases the fuel mass retained and subsequently the unique SPI. Thus, fuel properties that increase the energy needed to evaporate fuel off the liner increase the mass of fuel retained—a suspected SPI initiation source term—and accordingly, the measured unique SPI propensity also increases. Therefore, fuel

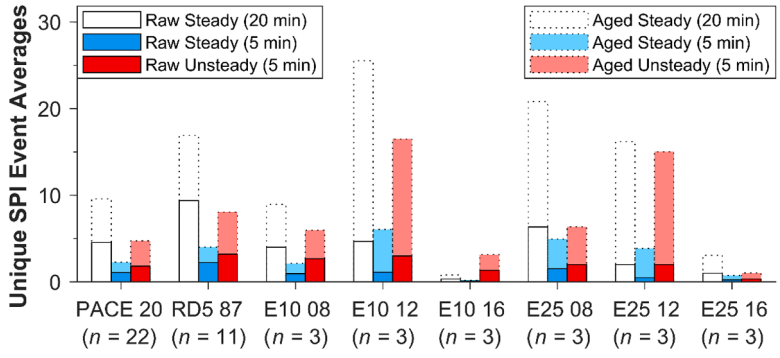

Fig. 21. Raw and age-adjusted unique SPI events are shown for unsteady (red), steady (white), and steady on a time-normalized basis (blue) portions of the test sequence, with age-adjusted totals in lighter, dotted bars.

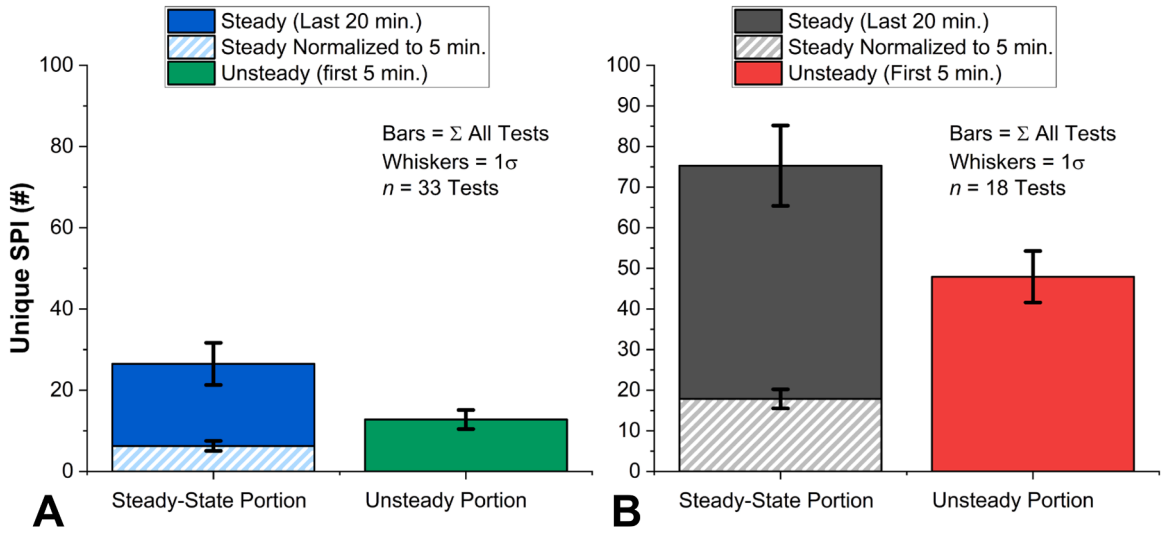

Fig. 22. (A) Steady and unsteady total SPI counts are shown for the control fuels, and (B) steady and unsteady SPI counts are shown for the test fuels.

properties and associated fuel retention are direct factors affecting unique SPI propensity at steady-state, high-load operation.

3.2. Unsteady engine operation results

3.2.1. SPI activity comparisons between steady and unsteady engine operation

The analysis thus far has centered on results at sustained steady-state operation. To explore if the steady-state results are consistent following low-to high load engine transients, the data were analyzed in separate steady-state (purple section in Fig. 3) and unsteady (green section in Fig. 3) partitions of the test sequence. Fig. 21 presents the average SPI of both the raw (solid bars) and age-adjusted data (dotted bars) for each fuel. In the figure, the white bars are averages for each fuel for the 20 min steady portion of operation. The red bars are averages for each fuel from the unsteady portion of the test (first 5 min, Fig. 3), and the blue bars are the steady-state results (white bars) divided by four to convert the 20 min steady-state data to a 5 min time-normalized basis equal to the unsteady test portion.

Results in Fig. 21 highlight that for all fuels, the average unique SPI in the unsteady portion (red bars) was more active than that in the time-normalized steady portion of the test (blue bars). This finding is significant because it suggests that the initial transition from low- to high-engine load could be more important in SPI than prior studies have indicated. The global effect of this observation is shown in Fig. 22, which presents the total unique SPI count (rather than the average, as shown in Fig. 21). The data in Fig. 22A represent the two control fuels (PACE 20 and RD 587), which have 33 tests in the grouping. Data in Fig. 22B show the total unique SPI count for the test fuels, which have 18 tests in the grouping.

Similar to the average unique SPI findings in Fig. 21, the total unique SPI count results in Fig. 22 depict that on a time-normalized basis, the unsteady portions of the 10-segment test (Fig. 3) were more active than the steady portions of the test. Additionally, Fig. 22 highlights that the

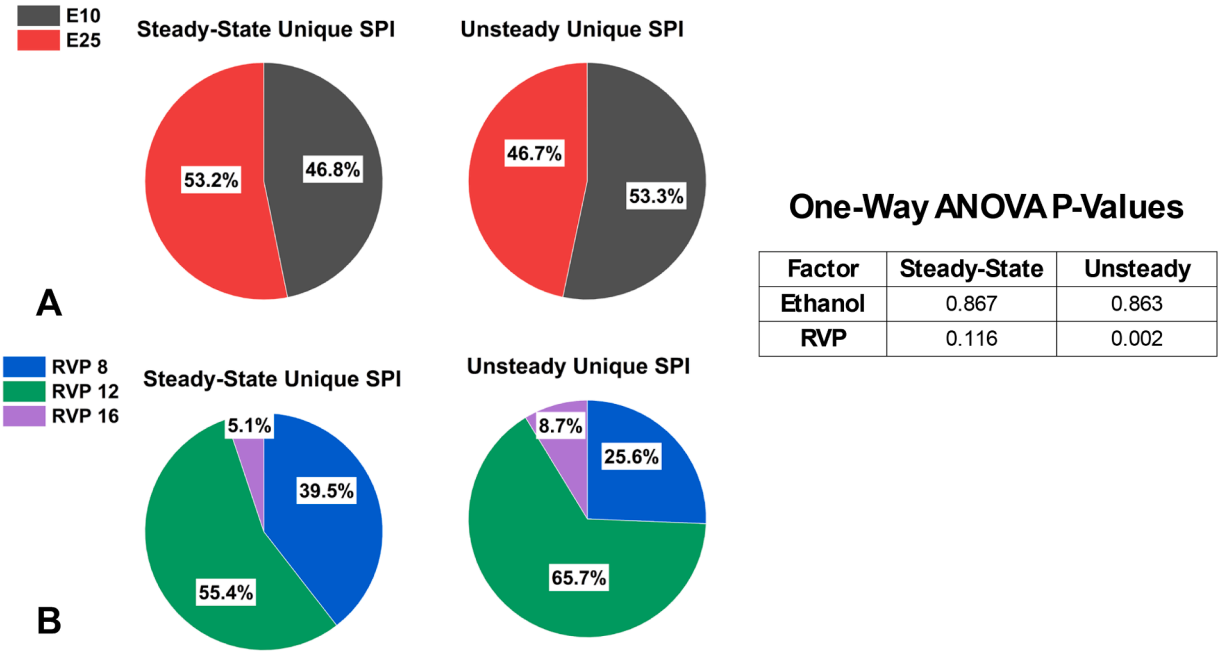

One-Way ANOVA P-Values

Factor	Steady-State	Unsteady
Ethanol	0.867	0.863
RVP	0.116	0.002

Fig. 23. SPI events in the steady and unsteady portions of the test sequence are grouped by (A) ethanol and (B) RVP.

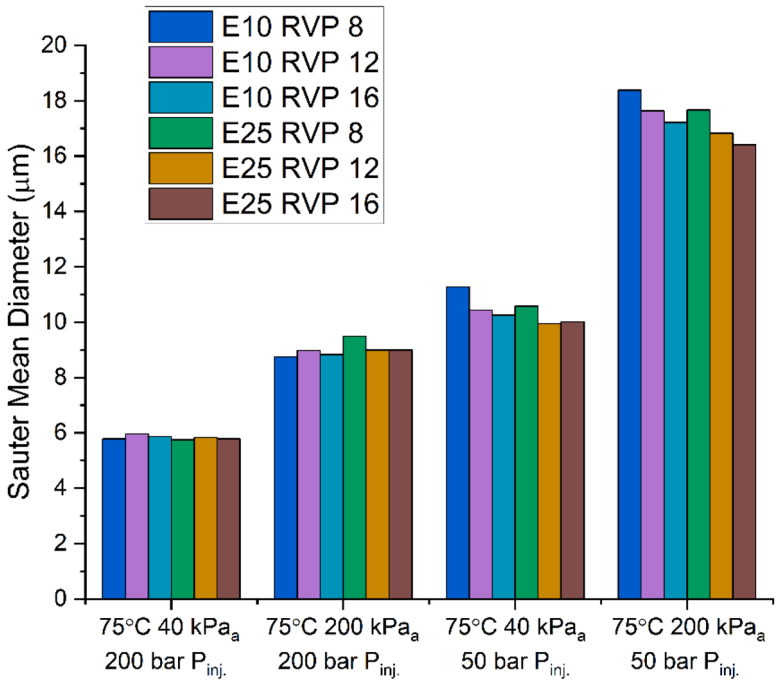

Fig. 24. The graph represents measured Sauter mean diameter for 75 °C fuel temperature at 40 and 200 kPa$_a$ ambient pressure and 50 and 200 bar injection pressure.

test fuels had approximately five times more SPI activity in the steady-state test portion compared with SPI activity in the control fuels (72 unique SPIs in 18 tests vs. 26 unique SPIs in 33 tests, yielding [72/18]/[26/33] = 5.1). Increased SPI activity in the test fuels was also observed in the unsteady portion of the test with approximately seven times more SPI activity in the test fuels compared with SPI activity in the control fuels (48 events in 18 tests vs. 13 events in 33 tests, yielding [48/18]/[13/33] = 6.8). Note that these results are adjusted for engine age according to the approach depicted in Fig. 2.

3.2.2. Fuel property significance quantification

Percentages of the total SPI events in steady-state and unsteady test periods attributed to the test fuels are plotted as pie charts in Fig. 23, with the fuels grouped by ethanol content (Fig. 23A) and RVP (Fig. 23B). Note that for Fig. 23A, a value of 50 % indicates that the property does not influence the result, and in Fig. 23B, a value of 33.3 % indicates no influence. The presented data are categorized using the approach outlined in Eq. (8), where x is either ethanol (Fig. 23A) or RVP (Fig. 23B), and n is 2 or 3 in the respective groupings.

$$relative\ effect = 100 \times \frac{total\ SPI_{x,i}}{\sum_1^n total\ SPI_{x,i}} \tag{8}$$

The analysis in Fig. 23A shows that ethanol had no direct influence on SPI propensity in either the steady or unsteady portion of the test sequence, with an approximately equal number of events occurring for both the E10 and E25 fuels. However, Fig. 23B shows that when analyzed as a function of RVP, a noticeable influence on both the steady-state and unsteady portions of the test occurred. RVP 12 displayed the highest SPI propensity in both portions of the test, resulting in double the factor that would be anticipated from no influence of RVP on unique SPI in the unsteady portion (i.e., 66.6 % vs. 33.3 %).

Based on the findings of Fig. 23, RVP could be a significant factor on SPI tendency. The significance of RVP in the steady or unsteady portions was determined and quantified using four separate one-way analysis of variance (ANOVA) tests, one each for ethanol and RVP in both steady and unsteady portions. All ANOVA were determined at a significance level of 0.05. The ANOVA results in Fig. 23 show that RVP in the unsteady portion of the test is the only data that meet the rejection of the null hypothesis, indicating that this grouping demonstrates statistical significance (i.e., RVP in the unsteady portion was found to affect SPI).

3.2.3. Off-engine fuel spray vessel measurement and quantification

The SPI ANOVA results in Fig. 23 provide evidence that fuel RVP is linked to SPI when low- to high-load transitions occur. Based on this finding and knowing that fuel volatility and temperature can affect fuel spray collapse at low loads, researchers suspected that RVP could be an indicator of fuel spray differences and spray collapse. To probe this theory, constant volume chamber spray imaging was conducted at three fuel temperatures, two injection pressures, and two ambient chamber pressures. Under each condition, Sauter mean diameter (SMD) of the droplets, fuel spray patterns, and tip penetration were characterized. The full suite of data is documented in Splitter, et al. (2023) [60], where the present analysis explored only representative low- and high-load conditions at 40 °C and 75 °C fuel temperatures, respectively, and the 75 °C fuel temperature was the only condition under which spray collapse and flash boiling were observed.

At the 75 °C fuel temperature condition, the SMD of the fuel sprays for 40 and 200 kPa$_a$ chamber pressure at 50 and 200 bar fuel injection pressure are presented in Fig. 24. The trends logically show that as fuel injection pressure increases, the SMD decreases. The data also show no significant difference in SMD with respect to any of the fuels at any condition except for the 200 bar injection pressure at 200 kPa$_a$ chamber pressure, where increasing both ethanol content and fuel RVP reduced SMD by an absolute maximum of only 2 μm. Thus, the SMD results suggest no significant droplet differences among the fuels at the explored spray characterization conditions.

Like the SMD results at 75 °C fuel temperature, the still images of the spray evolution and associated spray patterns at 50 mm from the injector tip for all fuels at 40 °C are presented in Fig. 25, showing no significant fuel effects at this fuel temperature. In Fig. 25, the left columns are the E25 fuels; the right columns are the E10 fuels; the first two rows are 200 bar injection pressure; and the bottom two rows are 50 bar injection pressure. Cases at 200 and 40 kPa$_a$ ambient chamber pressures are shown within the injection pressure subsets. Results show no obvious

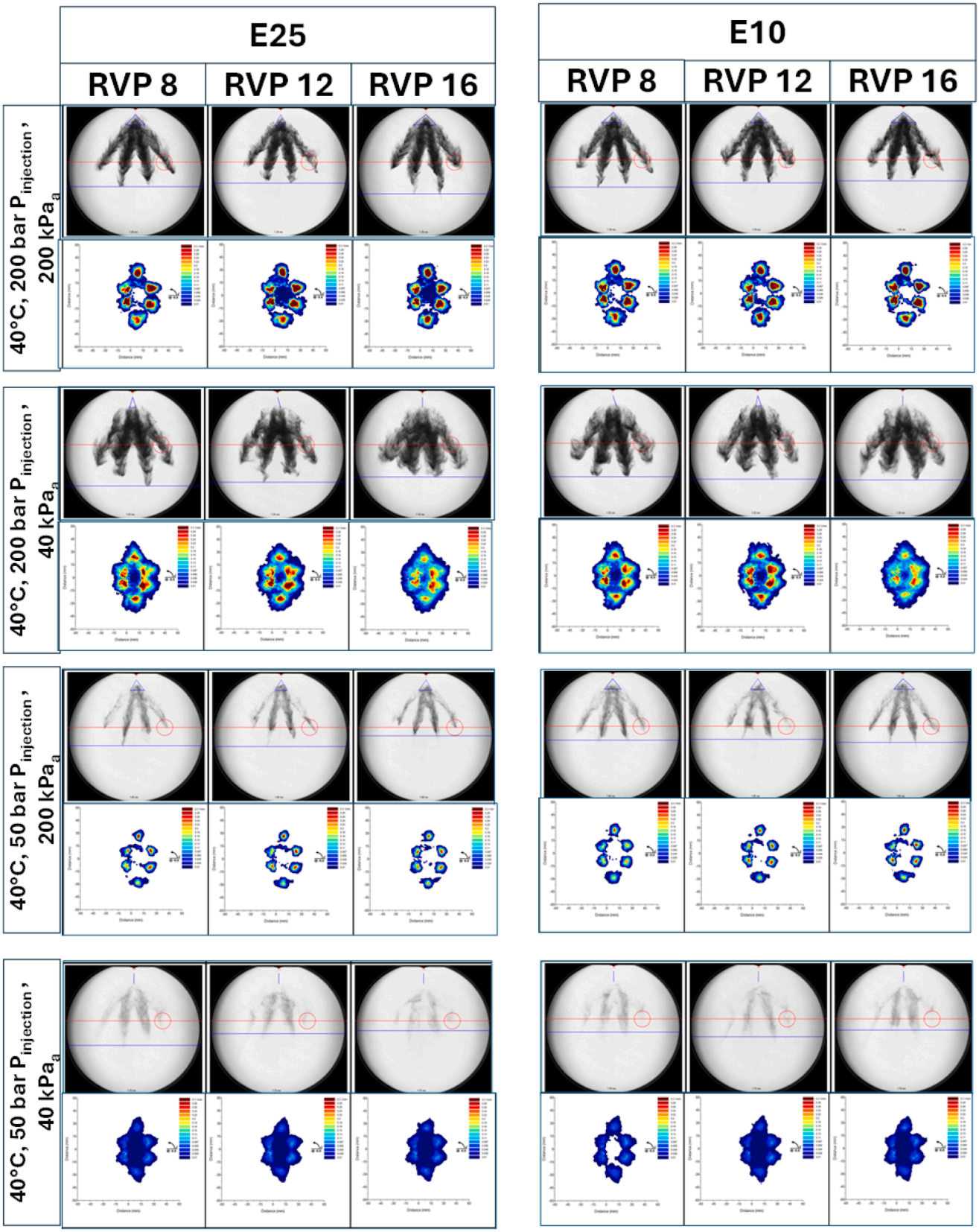

Fig. 25. Backlit still spray images and patterns are captured at 50 mm from the injector tip at a 40 °C fuel temperature.

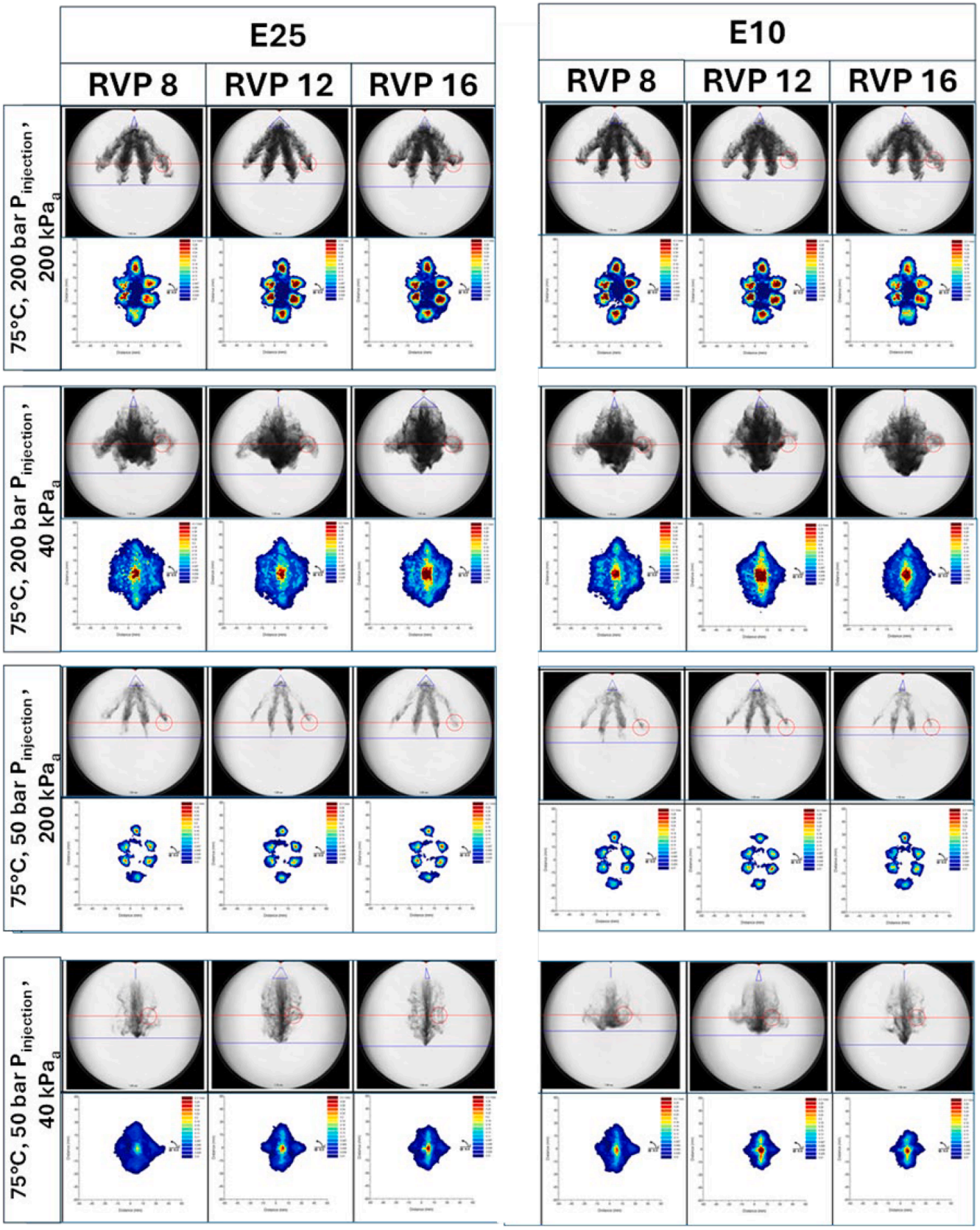

Fig. 26. Backlit still spray images and patterns are shown at 50 mm from the injector tip at a 75 °C fuel temperature.

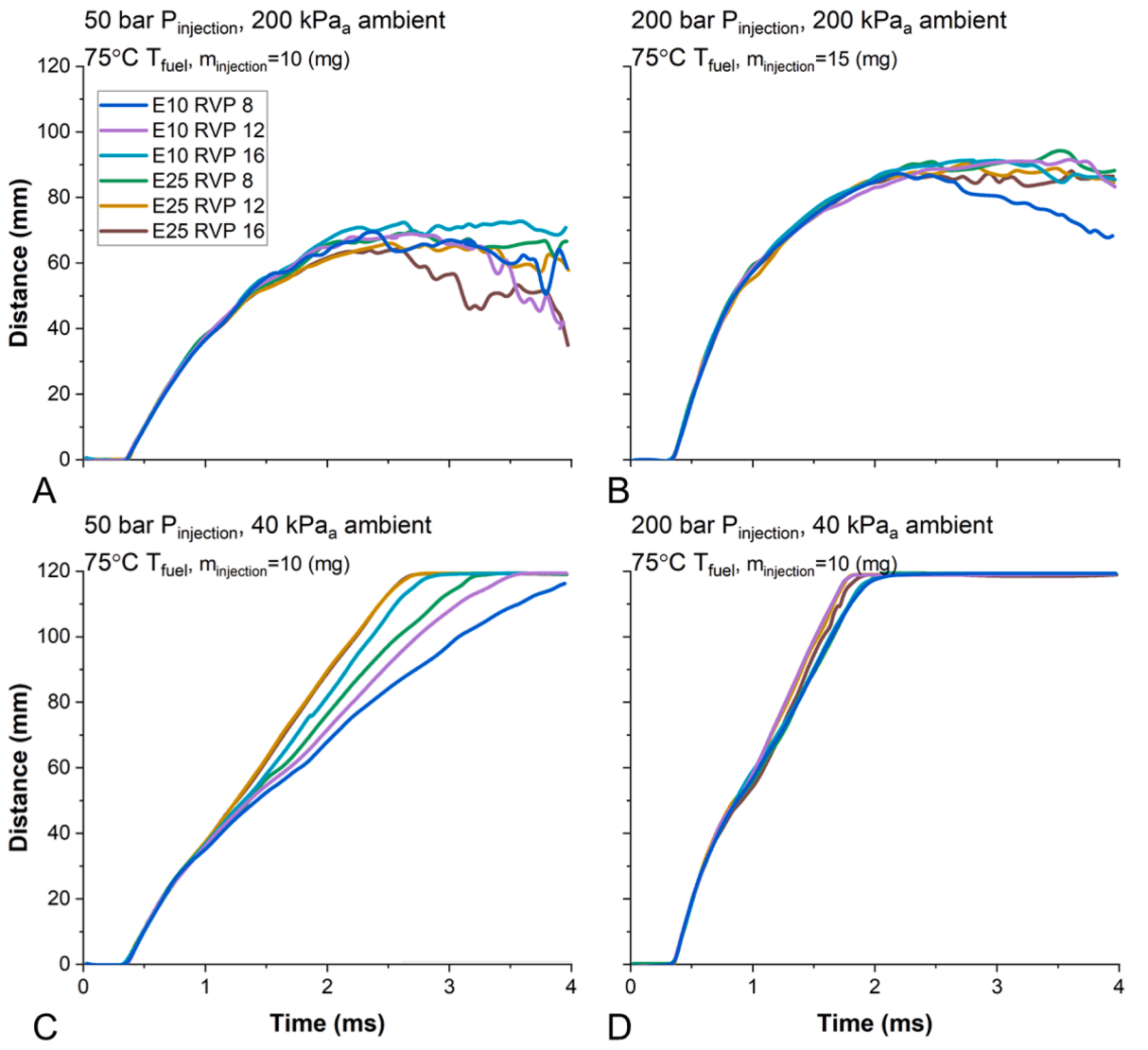

Fig. 27. Fuel spray penetration at the conditions from the patternation images in Fig. 26. Data in (A, B) depict spray penetration as a function of time for 200 kPa_a ambient pressure and (C, D) depict spray penetration at 40 kPa_a ambient (i.e., the collapsed spray conditions from Fig. 26). The left-hand column (A, C) is 50 bar injection pressure, and the right-hand column (B, D) is 200 bar injection pressure.

difference in the sprays over the range of conditions at 40 °C fuel temperature, with no fuels exhibiting spray collapse at these conditions and fuel temperature. Thus, fuel RVP was not observed to be a factor at this fuel temperature.

Fig. 26 shows the same sequence of spray images as shown in Fig. 25 but at an elevated fuel temperature of 75 °C vs. the prior 40 °C. When the fuel temperature increased from 40 °C to 75 °C, fuel RVP and ethanol differences became observable with respect to the spray penetration under some conditions. Unlike the highly similar spray results in Fig. 25, the more elevated fuel temperature results in Fig. 26 begin to show marked differences in fuel spray behaviors and patterns. This deviation is especially apparent at the 40 kPa_a condition, where evidence of spray collapse is clearly visible by the lack of individual spray plumes. Results show that in the collapsed sprays, the RVP 8 fuels have notionally the least collapsed sprays (central red area in the patternation images). Additionally, at the 200-bar injection pressure, the sprays have more defined jets—whether individual or collapsed—and the overall spray is larger in diameter. However, for the noncollapsed sprays, no significant RVP trend occurs in the red regions, suggesting that fuel RVP has no influence on the fuel plumes at the 200 kPa_a ambient chamber condition.

In the still images of Fig. 26, the blue lines denote the spray tip penetration at the time of the images. Notionally, only the 50-bar injection pressure had discernable differences in the location of the spray tip penetration when the still images were acquired. To better quantify spray penetration differences among the fuels, Fig. 27 plots the spray penetration of all the test fuels at the 40 and 200 kPa_a ambient chamber pressures and 50 and 200 bar injection pressure conditions for the 75 °C fuel.

Fig. 27A and 27B show the 75 °C fuel temperature spray penetration at 200 kPa_a chamber pressure (approximately the intake manifold pressure of the high-load portion of the test sequence, Fig. 3) for 50 and 200 bar injection pressure, respectively. At this non flash-boiling condition for a given injection pressure, the fuel penetrations were effectively the same for all the fuels. Note that the disparities past approximately 2 ms are caused by fuel evaporation and imaging artifacts. This suggests that at the high-load portion of the test, a difference in spray processes among the fuels is not expected.

Fig. 27C and 27D show the 75 °C fuel temperature spray penetration at 40 kPa_a chamber pressure (approximately equal to the intake manifold pressure during the low-load portion of the test sequence, Fig. 3) for 50 and 200 bar injection pressure, respectively. At the collapsing 40

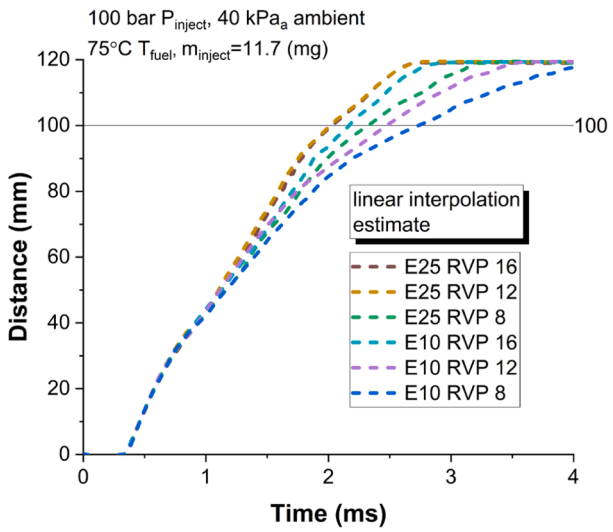

Individual Fuels	
Fuel	Time (ms)
E25 RVP 16	2.03
E25 RVP 12	2.04
E25 RVP 8	2.32
E10 RVP 16	2.17
E10 RVP 12	2.47
E10 RVP 8	2.73

Average Grouped by RVP	
Fuel	Time (ms)
μ RVP 16	2.10
μ RVP 12	2.25
μ RVP 8	2.53

Fig. 28. The estimated fuel spray penetration is calculated for the six test fuels at 100 bar injection at 40 kpa$_a$ ambient chamber pressure and 75 °C fuel temperature using linear interpolation of the 50 and 200 bar injection pressure measurements. Also tabulated is the time from start of injection required for the spray to impinge on the cylinder wall.

kPa$_a$ condition, the rate and severity of collapse were more dependent on fuel RVP and ethanol content at the lower injection pressure of 50 bar (Fig. 27C). At the higher rail pressure of 200 bar, all the fuels collapsed rapidly, and only minor differences were observed in spray penetration among fuels. This trend is meaningful because it establishes that fuel RVP and ethanol content matter at specific conditions. Moreover, in real-world applications, lower injection pressure is often required for lower fueling rates owing to limits on minimum injection duration and injector ballistics (i.e., spray targeting). At conditions beyond those shown here (e.g., higher fuel temperature, lower in-cylinder pressure, lower fuel injection pressure), fuel property effects on spray collapse could be even more exacerbated.

The combined results from Figs. 26 and 27 highlight that at intake conditions relevant to low engine loads (i.e., reduced in-cylinder pressure at the time of direct injection) with elevated fuel rail pressure, fuel RVP and ethanol content dependencies in the dynamics affecting spray collapse can exist. However, at intake conditions relevant to high-load operation, no significant spray differences were observed regardless of the fuel. The ramifications of these observations support the steady-state results where no fuel RVP effects were observed in the high-load, steady-state portion of the 10-segment test sequence (Fig. 3). However, the present analysis shown in Figs. 21 and 22 indicated that on a per-minute basis, significantly more SPI activity occurred in the first 5 min of high-load operation when the engine was at a thermally unsteady operating condition. Moreover, Fig. 23 confirmed that fuel RVP was a statistically significant factor in the unsteady portion of the test (the first 5 min of the 25 min high-load segment, Fig. 3). Combining these facts with the collapsing spray data in Figs. 25 and 26 elucidates the probable physical sources for the noted increases in SPI and fuel RVP dependency on SPI in the unsteady portion of the test.

Although not directly measured or controlled in the experiments, the inference is that the fuel temperature at low-load conditions could be elevated owing to the use of the production fuel rail (135 cc), which is four times larger than that needed for single-cylinder operation (i.e., the fuel rail was unmodified from the production four-cylinder engine). Based on the volume of the rail and single-cylinder fueling rate at the low-load portion of the test (approximately 15 g/min fuel flow), the fuel had an approximate 6.5 min residence time in the rail. At the high-load portion (approximately 85 g/min fuel flow), the fuel residence time decreased to approximately 1.2 min. Thus, the long residence time of the fuel in the rail at low load is assumed to result in an equilibrium between the fuel rail temperature and the coolant temperature (75 °C). This resulted in a delivered fuel temperature of approximately 75 °C during the low-load portion of the test. Therefore, the fuel temperature at the onset of the unsteady portion of the test possibly could be elevated and increased fuel-wall impingement could occur with higher RVP fuels during the low-load portion and during the low- to high-load transition of the test, thereby enabling *A. spi* source term to increase.

To test this hypothesis, the SPI and spray chamber results were combined to evaluate the data. Although engine testing in the present work employed a constant 100 bar injection pressure, the 100 bar injection pressure in the constant volume spray vessel work was not directly measured. However, 100 bar was bracketed by the 50 and 200 bar injection pressure cases shown in Figs. 25, 26, and 27. Note that the 200 bar injection pressure data was acquired at 15 mg/injection and the 50 bar injection pressure data was acquired at 10 mg/injection. Although matched fueling rates and only a pressure change would be ideal, these fueling rates also bracket the experimental fueling rate, which was approximately 14 mg/injection. Thus, to estimate the fuel spray penetration at 100 bar injection pressure, 75 °C fuel temperature, and 40 kPa$_a$ ambient chamber pressure (i.e., hot fuel at low load), a linear interpolation approach was employed to calculate the expected spray penetration. Results of the interpolation are presented in Fig. 28, and the resulting penetration time to 100 mm (representing the approximate free spray distance between the injector tip and cylinder liner) was calculated. The corresponding time to 100 mm for each test fuel on its own and the average of the fuels grouped as a function of RVP are also shown in Fig. 28. Note that only the lower 40 kPa$_a$ conditions were interpolated because the higher ambient pressure conditions do not spray collapse, and no significant fuel differences were observed. The data in Fig. 27C (and to a lesser extent, Fig. 27D) have penetration rates ordered with respect to RVP (i.e., the faster rate of collapse [left-most lines] are also the highest RVP fuels). These effects are also present in the interpolation of Fig. 28.

Results in Fig. 28 indicate that the E25 RVP 16 fuel is the fastest collapsing fuel, followed by E25 RVP 12, which has nearly the identical response. The fuels then order by E10 RVP 16, E25 RVP 8, E10 RVP 12, and finally E10 RVP 8.

3.2.4. *Coupling of off-engine fuel spray measurements to measured SPI propensity*

To quantify the effects of spray processes and fuel properties on SPI, the data were analyzed in the steady and unsteady portions of the test as both functions of the time to penetrate 100 mm at collapsing conditions

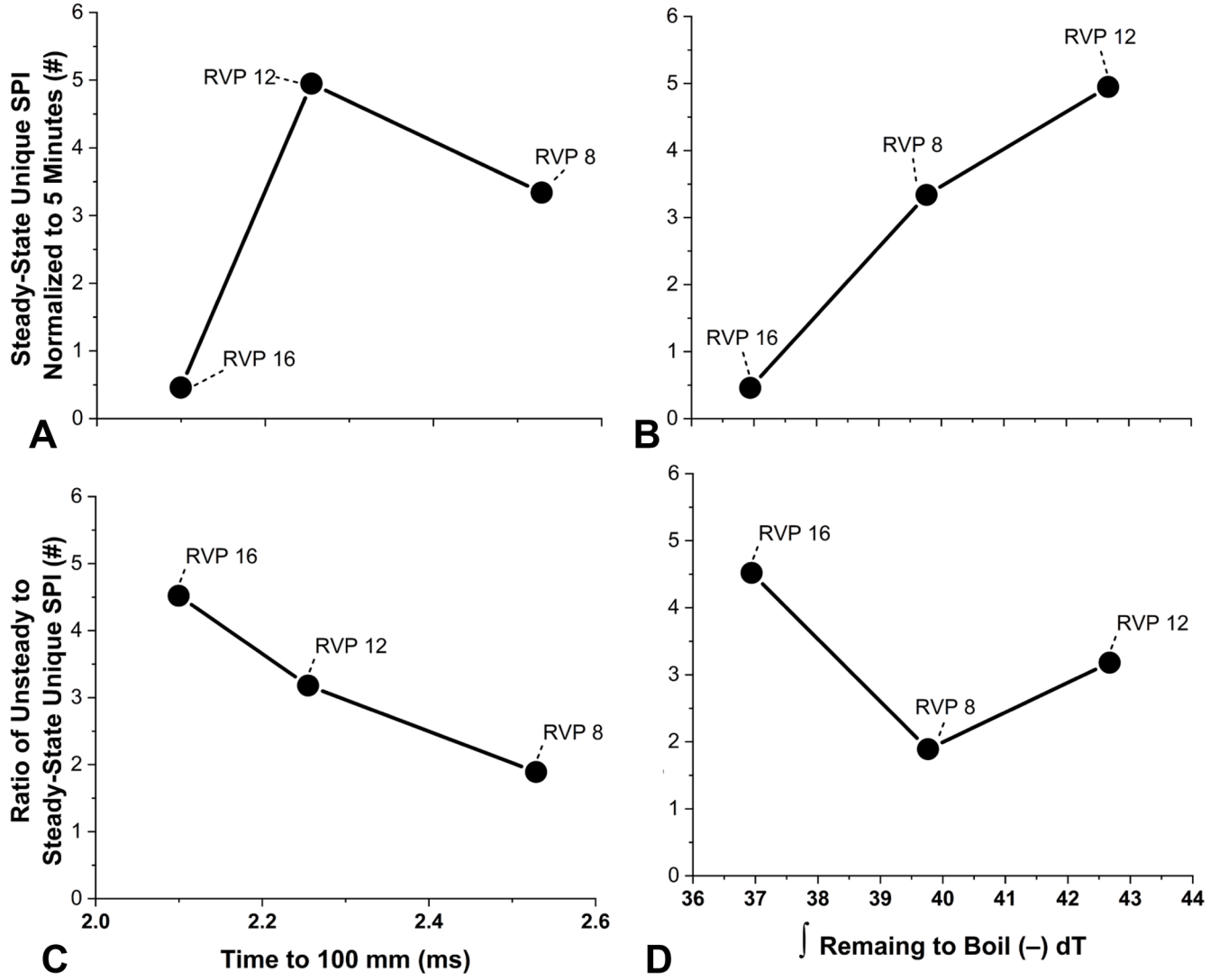

Fig. 29. (A) Steady-state unique SPI is normalized to a 5 min duration as a function of estimated penetration time to 100 mm (note no correlation exists in the data or with fuel RVP at this comparison). (B) Steady-state unique SPI is normalized to a 5 min duration as a function of fuel distillation (note the highly linear relation, yet no fuel RVP dependency exists in the steady-state condition). (C) Unsteady-state unique SPI is shown as a function of estimated penetration time to 100 mm (note the linear relationship with SPI in the unsteady portion with spray penetration and fuel RVP dependency). (D) Unsteady unique SPI is shown as a function of fuel distillation (note the lack of relation on fuel distillation or RVP).

and with respect to the fuel remaining to boil (Fig. 20). For each approach, the data were grouped as a function of RVP because Fig. 23 highlighted that RVP had the most significant effect on SPI tendency. The resulting analysis is presented in Fig. 29, with Fig. 29A and 29B showing results for the steady-state test portion and Fig. 29C and 29D showing results for the unsteady portion. The left column of the plots is the time to 100 mm for collapsing sprays, and the right column is the fuel remaining to boil above the liner temperature. Note that the spray penetration in the collapsing conditions occurred in the low-load portion of the test. Hence, the left-hand column in Fig. 29 is effectively plotting the influence of fuel properties in the low-load portion on SPI in the high-load portion of the test.

Results show two dominant effects. In Fig. 29B, the fuel remaining to boil is linearly correlated with unique SPI in the steady-state portion of the test. This suggests that fuel distillation is most critical to SPI, whereas RVP has no direct correlation at this operating condition. This finding is consistent with many literature studies, including Fig. 20 in the present work, meaning that fuel spray collapse is not a factor in SPI at steady-state boosted conditions because neither low-load fuel spray processes nor fuel RVP directly influence SPI (Fig. 29A).

However, when the unsteady portion of the test is analyzed, the fuel processes at low-load are important because fuel RVP and spray penetration rate are both correlated with unique SPI in the unsteady test portion (Fig. 29C). In this portion of the test, the boundary condition temperatures and trapped residuals were changing, and fuel distillation effects on SPI were weak (Fig. 29D). These observations indicate that in transient operation from low- to high-load transitions, fuel spray collapse that occurs at low loads can greatly influence SPI during these load transitions. This effect is even more important when considering effects of fuel RVP and seasonal fuel property variations, which exhibited a higher frequency of SPI in the unsteady portion of the test conducted in this study (Fig. 29C). These effects may be particularly relevant to real-world, in-vehicle applications in which rapid load transitions (e.g., high-speed merging and passing maneuvers) are more common than prolonged, steady-state operation at high engine loads.

4. Conclusions

This work highlighted that multiple fuel properties influence SPI, depending on the engine operating conditions. Steady-state high-load

engine operation data analysis highlighted that for sustained high-load engine operation, fuel distillation above the liner temperature is more significant to SPI propensity than fuel-wall impingement, ethanol content, or fuel RVP. That is, for sustained steady-state operation, no direct effect of fuel RVP or ethanol content between E10 and E25 on SPI was observed. Although fuel-wall impingement increased with E25 fuels relative to E10 fuels, the associated fuel retention was not found to be correlated to spray-wall impingement or SPI propensity. Fuel retention was found to be directly related to increasing the ASTM 7096 simulated distillation above the liner temperature, which correlated to the energy required to evaporate impinged fuel.

Interestingly, this study found that E25 compared with E10 increased fuel-wall impingement, but the resulting distillation for most of the E25 fuels reduced fuel retention of the impinged fuel at the sustained high-load operation. Fuel distillation, especially at temperatures above the liner temperature (approximately 100 °C for E10 and approximately 87 °C for E25), increased fuel retention. The two RVP 16 fuels were found to exhibit the lowest SPI rates for sustained high-load operation, whereas these fuels were found to require the lowest amount of energy to evaporate from above liner temperatures.

However, analyzing the unsteady low-to-high-load transition portion of the test cycle found that SPI was proportionally linked to fuel RVP, the opposite of the present steady-state sustained high-load work. In the field, sustained high-load engine operation is not as common as transient operation, including load transitions, which can be rapid. Thus, the unsteady engine operation results highlight that following abrupt engine load transitions, fuel spray collapse at low load could be a significant factor on subsequent high-load SPI propensity. Fuel RVP and ethanol content were explored as factors affecting fuel spray collapse. Findings in this work did not show a 95 % confidence interval significance between E10 and E25 fuels at RVP 8, 12, and 16 effects on unsteady SPI. However, when RVP effects were analyzed, increasing fuel RVP was found to proportionally increase SPI in the unsteady portion of the test. Higher RVP fuels exhibited faster spray penetration rates and thus increased fuel-wall impingement at low-load conditions. These results suggest that collapsing highly volatile sprays could affect SPI propensity following low- to high-load transitions.

Thus, the present work's findings elucidate that multiple fuel properties can influence SPI, where fuel distillation above the liner temperature was found to affect SPI at sustained high-load engine operation. However, fuel spray collapse and fuel RVP were found to influence SPI in more representative engine operation compared to real world use with rapid low-to-high-load engine transients. This bimodal dependency was consistent with fuel retention as ann SPI source, but the fuel properties to generate this source differed. This suggests that more than fuel distillation and sustained high-load engine operation alone should be examined when investigating SPI propensity of fuels and engines. Although the present results showed fuel RVP and biofuel content effects on SPI, the findings herein are not the only influencing factors on SPI or engine operation with these fuels. Additional factors relating to fuel effects on soot propensity and soot relations on SPI are areas for potential future work, which is beyond the current scope. These potential future areas could bolster the understanding of SPI more broadly regarding engine operation fuel properties and lubricant effects, all of which may be important and interdependent.

Funding

This research was conducted as part of the Co-Optimization of Fuels and Engines (Co-Optima) initiative sponsored by the US Department of Energy Office of Energy Efficiency and Renewable Energy and the Bioenergy Technologies and Vehicle Technologies Offices. Co-Optima is a collaborative project of multiple national laboratories initiated to simultaneously accelerate the introduction of affordable, scalable, and sustainable biofuels and high-efficiency, low-emission vehicle engines.

CRediT authorship contribution statement

Derek A. Splitter: Writing – review & editing, Writing – original draft, Visualization, Supervision, Investigation, Funding acquisition, Formal analysis, Data curation, Conceptualization. **Gurneesh Jatana:** Writing – review & editing, Investigation, Formal analysis, Data curation. **Dan DelVescovo:** Writing – review & editing, Writing – original draft, Formal analysis. **Gina Fioroni:** Writing – review & editing, Funding acquisition, Formal analysis, Conceptualization. **Elana Chapman:** Writing – review & editing, Supervision, Project administration, Funding acquisition, Conceptualization. **John Salyers:** Writing – review & editing, Formal analysis. **Johnathan Pung:** Writing – review & editing, Formal analysis. **Scott Parrish:** Writing – review & editing, Data curation.

Declaration of competing interest

The authors declare that they have no known competing financial interests or personal relationships that could have appeared to influence the work reported in this paper.

Acknowledgments

Special thanks to Vehicle Technologies Office program managers Kevin Stork, Gurpreet Singh, Leo Breton, and Mike Weismiller, as well as Bioenergy Technologies Office program manager Alicia Lindauer. We would also like to thank the Co-Optima Leadership Team, composed of John Farrell, Robert Wagner, John Holladay, Art Pontau, Dan Gaspar, Chris Moen, Bob McCormick, and Paul Bryan.

Data availability

Data will be made available on request.

References

[1] Jürgen W, Daniel M, Montefrancesco E, Geringer B, Hofmann P, Kieberger M. Limits on downsizing in spark ignition engines due to pre-ignition. MTZ Worldw 2009;70:56–61. https://doi.org/10.1007/BF03226955.
[2] Costanzo V, Yu X, Chapman E, Davis R. Fuel effects on the propensity to establish propagating flames *At spi*-relevant engine conditions. SAE Techn Pap 2021:0488. https://doi.org/10.4271/2021-01-0488. 2021-01-.
[3] Sasaki N, Nakata K, Kawatake K, Sagawa S, Watanabe M, Sone T. The effect of fuel compounds on pre-ignition under high temperature and high pressure condition. SAE Techn Pap 2011:1984. https://doi.org/10.4271/2011-01-1984. 2011-01-.
[4] Günther M, Tröger R, Kratzsch M, Zwahr S. Enthalpy-based approach to quantifying and preventing pre-ignition. MTZ Worldw 2011;72:42–7. https://doi.org/10.1365/s38313-011-0040-2.
[5] Zahdeh A, Rothenberger P, Nguyen W, Anbarasu M, Schmuck-Soldan S, Schaefer J, et al. Fundamental approach to investigate pre-ignition in boosted SI engines. SAE Int J Engines 2011;4(1):246–73. https://doi.org/10.4271/2011-01-0340.
[6] Jatana GS, Splitter DA, Kaul B, Szybist JP. Fuel property effects on low-speed pre-ignition. Fuel 2018;230:474–82. https://doi.org/10.1016/j.fuel.2018.05.060.
[7] Splitter D, Kaul B, Szybist J, Jatana G. Engine operating conditions and fuel properties on pre-spark heat release and SPI promotion in SI engines. SAE Int J Engines 2017;10(3):1036–50. https://doi.org/10.4271/2017-01-0688.
[8] Kalghatgi GT, Bradley D. Pre-ignition and "super-knock" in turbo-charged spark-ignition engines. Int J Engine Res 2012;13(4):399–414. https://doi.org/10.1177/1468087411431890.
[9] Splitter D, Kaul B, Szybist J, Speed L, Zigler B, Luecke J. Fuel-lubricant interactions on the propensity for stochastic pre-ignition. SAE Techn Pap 2019;1(24):0103. https://doi.org/10.4271/2019-24-0103. 2019-24-.
[10] Chapman E, Costanzo V. A literature review of abnormal ignition by fuel and lubricant derivatives. SAE Int J Engines 2016;9(1):107–42. https://doi.org/10.4271/2015-01-1869.
[11] Takeuchi K, Fujimoto K, Hirano S, Yamashita M. Investigation of engine oil effect on abnormal combustion in turbocharged direct injection - spark ignition engines. SAE Int J Fuels Lubr 2012;5(3):1017–24. https://doi.org/10.4271/2012-01-1615.
[12] Gohl M, Brandt S, Wittler M, Budde M, Knoll G, Krause S, et al. Influence of the mixture formation on the lubrication oil emission of combustion engines. SAE Int J Fuels Lubr 2010;3(1):733–44. https://doi.org/10.4271/2010-01-1275.
[13] Haenel P, Seyfried P, Kleeberg H, Tomazic D. Systematic approach to analyze and characterize preignition events in turbocharged direct-injected gasoline engines. SAE Techn Pap 2011:0343. https://doi.org/10.4271/2011-01-0343. 2011-01-.

[14] Kalghatgi G, Algunaibet I, Morganti K. On knock intensity and superknock in SI engines. SAE Int J Engines 2017;10(3):1051–63. https://doi.org/10.4271/2017-01-0689.

[15] Fletcher KA, Dingwell L, Yang K, Lam WY, Styer JP. Engine oil additive impacts on low speed pre-ignition. SAE Int J Fuels Lubr 2016;9(3):612–20. https://doi.org/10.4271/2016-01-2277.

[16] Ritchie A, Boese D, Young AW. Controlling low-speed pre-ignition in modern automotive equipment part 3: identification of key additive component types and other lubricant composition effects on low-speed pre-ignition. SAE Int J Engines 2016;9(2):832–40. https://doi.org/10.4271/2016-01-0717.

[17] Kocsis MC, Briggs T, Anderson G. The impact of lubricant volatility, viscosity and detergent chemistry on low speed pre-ignition behavior. SAE Int J Engines 2017;10(3):1019–35. https://doi.org/10.4271/2017-01-0685.

[18] Szybist JP, Busch S, McCormick RL, Pihl JA, Splitter DA, Ratcliff MA, et al. What fuel properties enable higher thermal efficiency in spark-ignited engines? Prog Energy Combust Sci 2021;82:100876. https://doi.org/10.1016/j.pecs.2020.100876.

[19] Kar A, Huisjen A, Aradi A, Reitz J, Iqbal A, Haumann K, et al. Assessing the impact of lubricant and fuel composition on LSPI and emissions in a turbocharged gasoline direct injection engine. SAE Int J Adv Curr Prac Mobil 2020;2(5):2568–80. https://doi.org/10.4271/2020-01-0610.

[20] Ohtomo M, Miyagawa H, Koike M, Yokoo N, Nakata K. Pre-ignition of gasoline-air mixture triggered by a lubricant oil droplet. SAE Int J Fuels Lubr 2014;7(3):673–82. https://doi.org/10.4271/2014-01-2627.

[21] Mayer M, Hofmann P, Geringer B, Williams J, Moss J, Kapus P. Influence of different oil properties on low-speed pre-ignition in turbocharged direct injection spark ignition engines. SAE Techn Pap 2016:0718. https://doi.org/10.4271/2016-01-0718. 2016-01-.

[22] Splitter D, Colomer VB, Neupane S, Chuahy FDF, Jr Partridge W. In situ laser induced fluorescence measurements of fuel dilution from low load to stochastic pre ignition prone conditions. SAE Techn Pap 2021:0489. https://doi.org/10.4271/2021-01-0489. 2021-01-.

[23] Splitter D, Colomer VB, Neupane S, Jr Partridge W. Fuel properties effects on wall-wetting and fuel-in-lube dilution under stochastic pre ignition prone conditions. In: Proceedings of the 12th US national combustion meeting; 2021. May24–26.

[24] Neupane S, Boronat V, Splitter D, Partridge WP. An improved method for determining transient fuel dilution of oil in an internal-combustion engine using laser-induced fluorescence and multivariate least square calibration. Appl Spectrosc 2021;75(10):1237–50. https://doi.org/10.1177/0003702821996455.

[25] Parks J, Partridge B, Whitacre S. Rapid in situ measurement of fuel dilution of oil in a diesel engine using laser-induced fluorescence spectroscopy. SAE Techn Pap 2007:4108. https://doi.org/10.4271/2007-01-4108. 2007-01-.

[26] Gasoline reid vapor pressure. United States Environmental Protection Agency; 2024. https://www.epa.gov/gasoline-standards/gasoline-reid-vapor-pressure [accessed January 2025].

[27] Date of switch to summer-grade gasoline approaches. U.S. Energy Information Administration; 2013. https://www.eia.gov/todayinenergy/detail.php?id=11031#:~:text=For%20logistical%20reasons%2C%20the%20transition,use%20for%20a%20longer%20period [accessed July 2025].

[28] Gasoline sampling and analysis to investigate the effect of reid vapor pressure on vapor recovery system overpressure. California Air Resources Board; 2017. https://ww2.arb.ca.gov/sites/default/files/2020-10/VR-OP-G1%20FINAL.pdf [accessed July 2025].

[29] Regulatory advisory. California Air Resources Board; 2023. September 28, https://ww2.arb.ca.gov/sites/default/files/2023-09/RVP_Advisory_2023.pdf. 2023 [accessed July 2025].

[30] U.S. gasoline prices decline amid lower gasoline demand and falling crude oil prices. U.S. Energy Information Administration; 2023. https://www.eia.gov/todayinenergy/detail.php?id=61003 [accessed July 2025].

[31] Regulatory advisory. California Air Resources Board; 2022. September 30, https://ww2.arb.ca.gov/sites/default/files/2022-09/RVP%20Advisory%202022.pdf. 2022 [accessed July 2025].

[32] Andersen VF, Anderson JE, Wallington TJ, Mueller SA, Nielsen OJ. Vapor pressures of alcohol−gasoline blends. Energy Fuels 2010;24(6):3647–54. https://doi.org/10.1021/EF100254W.

[33] Methanol use in gasoline: blending, storage and handling of gasoline containing methanol. Methanol blending technical product bulletin. Methanol Institute; 2016. https://www.methanol.org/wp-content/uploads/2016/06/Blending-Handling-Bulletin-Final.pdf [accessed July 2025].

[34] Gaspar DJ, Phillips SD, Polikarpov E, Albrecht KO, Jones SB, George A, et al. Measuring and predicting the vapor pressure of gasoline containing oxygenates. Fuel 2019;243:630–44. https://doi.org/10.1016/j.fuel.2019.01.137.

[35] E15 Reid vapor pressure fuel waiver. United States Environmental Protection Agency; 2024. https://www.epa.gov/system/files/documents/2024-05/e15extensionreidvapor-fuelwaiver052124.pdf. 2024 [accessed July 2025].

[36] Final rule in response to request from states for removal of gasoline volatility waiver. United States Environmental Protection Agency; 2025. https://www.epa.gov/gasoline-standards/final-rule-response-request-states-removal-gasoline-volatility-waiver [accessed July 2025].

[37] Rönn K, Swarts A, Kalaskar V, Alger T, Tripathi R, Keskiväli J, et al. Low-speed pre-ignition and super-knock in boosted spark-ignition engines: a review. Prog Energy Combust Sci 2023;95:101064. https://doi.org/10.1016/j.pecs.2022.101064.

[38] Singh E, Dibble R. Knock auto-ignition and pre-ignition tendency of fuels for advanced combustion engines (FACE) with ethanol blends and similar RON. SAE Techn Pap 2020:0613. https://doi.org/10.4271/2020-01-0613. 2020-01-.

[39] Haenel P, Kleeberg H, de Bruijn R, Tomazic D. Influence of ethanol blends on low speed pre-ignition in turbocharged, direct-injection gasoline engines. SAE Int J Fuels Lubr 2017;10(1):95–105. https://doi.org/10.4271/2017-01-0687.

[40] Costanzo VS, Yu X, Chapman E, Davis R, Haenel P. Fuel & lubricant effects on stochastic preignition. SAE Int J Adv Curr Prac Mobil 2019;1(1):259–77. https://doi.org/10.4271/2019-01-0038.

[41] Mayer M, Hofmann P, Geringer B, Williams J, Moss J. Influence of different fuel properties and gasoline-ethanol blends on low-speed pre-ignition in turbocharged direct injection spark ignition engines. SAE Int J Engines 2016;9(2):841. https://doi.org/10.4271/2016-01-0719. –8.

[42] Splitter D, Colomer VB, Neupane S, Partridge W. Engine operating conditions, fuel property effects, and associated fuel–wall interaction dependencies of stochastic preignition. SAE Techn Pap 2023:1615. https://doi.org/10.4271/2023-01-1615. 2023-01-.

[43] Chupka GM, Christensen E, Fouts L, Alleman TL, Ratcliff MA, McCormick RL. Heat of vaporization measurements for ethanol blends up to 50 volume percent in several hydrocarbon blendstocks and implications for knock in SI engines. SAE Int J Fuels Lubr 2015;8(2):251–63. https://doi.org/10.4271/2015-01-0763.

[44] Kouchi S, Okamoto S, Ozawa K, Kawashima H, Ishima T, Uchida R, et al. Observation and analysis of behavior of spray impingement on a liquid film. SAE Techn Pap 2015:2006. https://doi.org/10.4271/2015-01-2006. 2015-01-.

[45] Moriyoshi Y, Kuboyama T, Takaki T, Hitosugi H. Investigation on relationship between LSPI and lube oil consumption and its countermeasure. SAE Techn Pap 2021:0567. https://doi.org/10.4271/2021-01-0567. 2021-01-.

[46] Michlberger A, Sutton M, Kocsis M, Anderson G, Van Horn A. On-road monitoring of low speed pre-ignition. SAE Techn Pap 2018:1676. https://doi.org/10.4271/2018-01-1676. 2018-01-.

[47] Haenel P, Seyfried P, Kleeberg H, Tomazic D. Systematic approach to analyze and characterize preignition events in turbocharged direct-injected gasoline engines. SAE Techn Pap 2011:0343. https://doi.org/10.4271/2011-01-0343. 2011-01-.

[48] Relf J, Petrovich S, Ebrahimi K. Biofuel concentration in low-speed pre-ignition in gasoline engines. Fuels 2024;5(2):243–60. https://doi.org/10.3390/fuels5020014.

[49] Sakai S, Shen A, Rothamer D. Comparison of ethanol-, isobutanol-, and 2-methyl-3-buten-2-ol–gasoline sprays from a gasoline direct injector. Fuel 2024;355:129319. https://doi.org/10.1016/j.fuel.2023.129319.

[50] Zeng W, Xu M, Zhang G, Zhang Y, Cleary DJ. Atomization and vaporization for flash-boiling multi-hole sprays with alcohol fuels. Fuel 2012;95:287–97. https://doi.org/10.1016/j.fuel.2011.08.048.

[51] Wu S, Yang S, Wooldridge M, Xu M. Experimental study of the spray collapse process of multi-hole gasoline fuel injection at flash boiling conditions. Fuel 2019;242:109–23. https://doi.org/10.1016/j.fuel.2019.01.027.

[52] Araneo L, Donde R. Flash boiling in a multihole G-DI injector—effects of the fuel distillation curve. Fuel 2017;191:500–10. https://doi.org/10.1016/j.fuel.2016.11.104.

[53] Hwang J, Weiss L, Karathanassis IK, Koukouvinis P, Pickett LM, Skeen SA. Spatio-temporal identification of plume dynamics by 3D computed tomography using engine combustion network spray G injector and various fuels. Fuel 2020;280:118359. https://doi.org/10.1016/j.fuel.2020.118359.

[54] Neupane S, Boronat CV, Splitter D, Partridge W. Measurement of engine-oil fuel dilution using laser induced fluorescence spectroscopy. In: Proceedings of the 2020 spring technical meeting central states section of the combustion institute; 2020. May 17–19.

[55] Splitter DA, Szybist JP. Experimental investigation of spark-ignited combustion with high-octane biofuels and EGR. 1. engine load range and downsize downspeed opportunity. Energy Fuels 2013;28(2):1418–31. https://doi.org/10.1021/ef401574p.

[56] Kalaskar VB, Swarts A, Alger T. Impact of engine age and engine hardware on low-speed pre-ignition. SAE Techn Pap 2018:1663. https://doi.org/10.4271/2018-01-1663. 2018-01-.

[57] Szybist JP, Splitter DA. Impact of engine pressure-temperature trajectory on autoignition for varying fuel properties. Appl Energy Combust Sci 2020;1:100003. https://doi.org/10.1016/j.jaecs.2020.100003.

[58] Mansfield AB, Chapman E, Briscoe K. Impact of fuel octane rating and aromatic content on stochastic pre-ignition. SAE Techn Pap 2016:0721. https://doi.org/10.4271/2016-01-0721. 2016-01-.

[59] Wagnon SW. Development of an optimized gasoline surrogate formulation for pace experiments and simulations. Livermore (CA): Lawrence Livermore National Laboratory; 2020. https://doi.org/10.2172/1960480. Report No.: LLNL-TR-816442. Contract No.: AC52-07NA27344. Sponsored by the USDOE National Nuclear Security Administration (NNSA.

[60] Splitter D., Jatana G., Fioroni G., Chapman E., Salyers J. Bio-fuel effects and seasonal fuel property variations related to abnormal combustion occurrences observed in the field. Oak Ridge (TN): Oak Ridge National Laboratory; 2023 Sep. Report No.: ORNL/SPR-2023/3002. Contract No.: DE-AC05-00OR22725.

[61] ASTM D7096. Standard test method for determination of the boiling range distribution of gasoline by wide-bore capillary gas chromatography. ASTM Book of Stand; 2019. https://doi.org/10.1520/D7096-19. 05.03.

[62] Wagnon SW, Cheng S, Goldsborough SS, Kukkadapu G, Lapointe S, McNenly MJ, et al. Chemical kinetic models for surrogate fuels. In: Proceedings of the 2021 DOE vehicle technologies office annual merit review; 2021. https://www.energy.gov/sites/default/files/2021-06/ace139_wagnon_2021_o_5-15_140am_KS_LS.pdf.

[63] Mills ZG, Finney CE, Haynes JA, Trofimov AA, Wang H, Pierce DT. Impact of materials properties on higher-temperature engine operation. SAE Techn Pap 2021:1142. https://doi.org/10.4271/2021-01-1142. 2021-01-.